Cortico-thalamo-cortical interactions modulate electrically evoked EEG responses in mice

AUTHORS

Leslie D. Claar[1†]*, Irene Rembado[1†]*, Jacqulyn R. Kuyat[1], Simone Russo[1,2], Lydia C. Marks[1], Shawn R. Olsen[1], Christof Koch[1]*

[1] MindScope Program, Allen Institute, Seattle, United States

[2] Department of Biomedical and Clinical Sciences "L. Sacco", University of Milan, Milan, Italy

[†] These authors contributed equally to this work.

* Correspondence: lesliec@alleninstitute.org, irene.rembado@alleninstitute.org, christofk@alleninstitute.org

ABSTRACT

Perturbational complexity analysis predicts the presence of consciousness in volunteers and patients by stimulating the brain with brief pulses, recording electroencephalographic (**EEG**) responses, and computing their spatiotemporal complexity. We examined the underlying neural circuits in mice by directly stimulating cortex while recording with EEG and Neuropixels probes during wakefulness and isoflurane anesthesia. When mice are awake, stimulation of deep cortical layers reliably evokes locally a brief pulse of excitation, followed by a bi-phasic sequence of 120 ms profound *off* period and a *rebound* excitation. A similar pattern, partially attributed to burst spiking, is seen in thalamic nuclei, and is associated with a pronounced late component in the evoked EEG. We infer that cortico-thalamo-cortical interactions drive the long-lasting evoked EEG signals elicited by deep cortical stimulation during the awake state. The cortical and thalamic off period and rebound excitation, and the late component in the EEG, are reduced during running and absent during anesthesia.

INTRODUCTION

A long-standing clinical challenge has been to discover sensitive and specific biomarkers of consciousness. One obvious candidate is electroencephalography (**EEG**), with high amplitude delta activity usually taken as an indicator of absence of consciousness, as during deep sleep, anesthesia, in vegetative state patients (also known as behavioral unresponsive wakefulness syndrome), or in coma (Bai et al., 2017; Kobylarz & Schiff, 2005; Schiff et al., 2014). However, given the vast diversity of patients and their etiology, spontaneous EEG can show very unusual spatio-temporal patterns, with attendant high false alarm and miss rates in diagnosing individual patients with disorders of consciousness (Farisco et al., 2022; Frohlich et al., 2021; Thibaut et al., 2019). More promising is the perturbational EEG (Bai et al., 2021), in which the brain is probed by a brief pulse (generated via transcranial magnetic stimulation, **TMS**, applied to the skull or electrical stimulation applied intracranially) and the resulting cortical activity is recorded using a high-density EEG electrode array or stereo-EEG electrodes (Casali et al., 2013; Casarotto et al., 2016; Comolatti et al., 2019; Massimini et al., 2005; Pigorini et al., 2015; Rosanova et al., 2018). A simple algorithm then computes the *perturbational complexity index* (**PCI**) of the brain's reverberations to this pulse from which the presence of consciousness can be inferred with unprecedented sensitivity (low false alarm rate), and specificity (low miss rate), at the level of individual patients (Bai et al., 2021; Kondziella et al., 2020).

PCI has been comprehensively studied and validated in humans since its introduction by Massimini and colleagues in 2005 (Casali et al., 2013; Casarotto et al., 2016; Comolatti et al., 2019; Ferrarelli et al., 2010; Massimini et al., 2005; Rosanova et al., 2018). Pigorini et al. (2015) proposed that during non-rapid eye movement (**NREM**) sleep, when the brain is characterized by cortical bistability, neurons tend to fall into a down-state following activation (either endogenous or exogenous) preventing extended causal interactions that are typical during wakefulness (Hill & Tononi, 2005; Rosanova et al., 2018; Timofeev et al., 2001).

Limitations in access to high resolution cellular recordings in humans have motivated recent efforts to translate the PCI technique to model systems for more detailed studies of the circuit mechanisms underlying complexity changes. In 2018, D'Andola et al. demonstrated that an approximation of PCI developed for *in vitro* measurements captured complexity differences in ferret cortical slices exhibiting sleep- and awake-like activity patterns. They showed that during a sleep-like state, electrical stimulation induced a down-state that disrupted the complex pattern of activation observed in the awake-like state (D'Andola et al., 2018). Arena et al. (2021) were the first to recapitulate the human PCI results *in vivo* in rodents; they computed the complexity of electrically evoked EEG responses in rats and showed that PCI was high during wakefulness and low during anesthesia. In their comprehensive study, they found that in the anesthetized state (via propofol or sevoflurane), stimulation was followed by a widespread suppression of high frequencies in the EEG responses, suggestive of a down-state, in agreement with previous findings (D'Andola et al., 2018; Pigorini et al., 2015). Dasilva et al. (2021) measured PCI *in vivo* in anesthetized mice and showed that complexity can be modulated even within the anesthetized state. They showed that PCI was highest for mice under light isoflurane anesthesia (defined as a concentration of 0.1%), decreasing systematically at medium (0.34%) and deep (1.16%) concentrations. Recently, Cavelli, Mao et al. (2022) validated the use of PCI in freely moving rodents across wakefulness, both REM and NREM sleep, and anesthesia by demonstrating that PCI calculated on cortical laminar local field potential (**LFP**) signals decreases in unconscious states (both natural and induced) in rats and mice. While pioneering, none of these studies simultaneously recorded micro- and macro-signals – neurons and LFP at hundreds of sites, together with EEG.

To investigate how cortico-cortical and cortico-thalamic activity influences the complexity of the evoked responses, we used EEG simultaneously with Neuropixels probes (Jun et al., 2017) to record brain-wide evoked responses to cortical electrical stimulation in head-fixed mice that were awake and, subsequently, anesthetized with isoflurane. Due to their ability to record spiking and LFP signals from

hundreds of sites across cortical layers and subcortical structures at 20 µm resolution, Neuropixels probes provide unprecedented access to the intra- and interareal dynamics that underlie the macro-scale EEG signals. We show that cortical stimulation elicits a widespread, complex event-related potential (**ERP**) in the EEG signals in the awake state, but a much simpler ERP in the isoflurane-anesthetized state, in agreement with what has been shown in humans (Casali et al., 2013) and rodents (Arena et al., 2021; Cavelli et al., 2022). We demonstrate a stereotyped pattern of activity to stimulation in deep (but not superficial) cortical layers – brief excitation, followed by a profound *off* period and a *rebound* excitation ("rebound" is a term often used to describe a period of enhanced spiking following a period of inhibition or silence [Grenier et al., 1998; Guido & Weyand, 1995; Roux et al., 2014]). This sequence is repeated in the thalamus, supported by burst firing in excitatory thalamic neurons. Based on relative timing between cortical and thalamic evoked activity, we infer that thalamic bursting is necessary for the late, evoked EEG component seen in response to electrical stimulation, a novel result that links the ERP to activity in the cortico-thalamo-cortical (**CTC**) loop.

RESULTS

Global evoked responses are modulated by the depth of the cortical stimulation site

We recorded global EEG-like neural signals using a multi-electrode surface array on the skull, but below the scalp (Jonak et al., 2018; Land et al., 2019), in head-fixed mice. The multi-electrode array consisted of 30 electrodes situated over primary and secondary motor, somatosensory, visual, and retrosplenial areas in both hemispheres (Figure 1A). We used an average reference montage that removed signals common to all EEG electrodes (see Methods). We inserted a bipolar wire electrode intra-cortically to repeatedly deliver a single electrical current pulse into the cortex and measured the evoked potentials with the EEG array (Figure 1B and 1C). The current pulses were biphasic with an amplitude between 10-100 µA (details in Figure 1C inset). Stimulation artifacts in the EEG signals were reduced by replacing the

signal between 0 and +2 ms following each stimulus with the signal between -2 and 0 ms; this was done to all traces in all trials during an offline, signal pre-processing step. All subsequent analysis of the ERP (the trial-averaged EEG response) excludes the signal between -2 and +2 ms. During the experiment, we closely observed the animal for signs of electrically evoked motor twitches and chose lower stimulation amplitudes if we observed any.

To understand how the features of the ERP depend on the location of the electrical stimulation, we varied both the area and the depth (or cortical layer) of the stimulating electrode. We stimulated in the secondary motor area (**MOs**) and the primary somatosensory area (**SSp**) in layer 2/3 (superficial: 0.41±0.04 mm below the brain surface) and layer 5/6 (deep: 1.06±0.05 mm below the brain surface) (Figure 1D). We found that regardless of area, when we stimulated layer 5/6 during the awake period, we usually observed two prominent peaks in the ERP: an initial response around 25 ms and secondary peak at around 180 ms post-stimulation (Figure 1C and 1D).

The early component was preserved, whereas the second, late component was not evident when stimulating superficially in either area (Figure 1D). The total duration of the ERP was shorter when stimulating superficial layers compared to deep layers although not significant (mean ERP duration for superficial stimulation: 0.4±0.0 s; deep stimulation: 0.5±0.1 s; Student's two-tailed t-test, p=0.0843; Figure 1E, Figure 1-figure supplement 1). When stimulating superficially, ERPs had a significantly smaller normalized magnitude compared to stimulating deep layers (mean ERP magnitude for superficial stimulation: 3.3±0.8 s.d.·s; deep stimulation: 6.2±0.9 s.d.·s; Student's two-tailed t-test, p=0.0354; Figure 1F, Figure 1-figure supplement 1).

The amplitude of the first peak in the ERP decays systematically when moving away from the stimulation site until it eventually flips its sign, most likely reflecting volume conduction (Figure 1-figure supplement

2). The magnitude and polarity of the second component likewise changes continuously but in a different pattern, suggesting a different mechanistic origin.

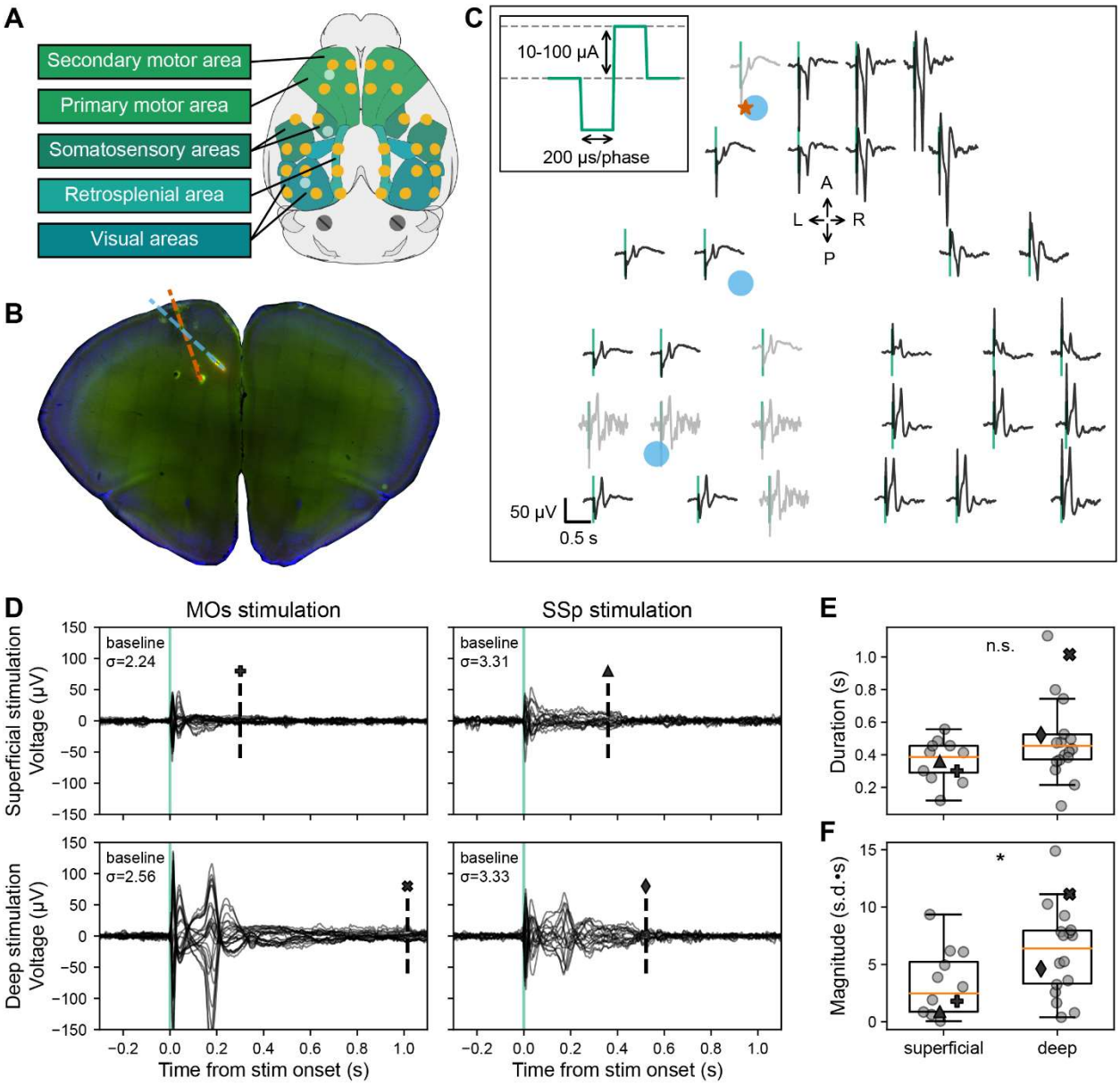

Figure 1: Evoked EEG responses to single pulse electrical stimulation in awake, head-fixed mice.

(A) Schematic of the 30-channel surface array (yellow circles) implanted on top of the skull over major brain areas: motor, somatosensory, retrosplenial, and visual areas (schematic created using *brainrender*, Claudi et al., 2021).

The circular, platinum EEG electrodes are 500 µm in diameter. The three light blue circles correspond to the locations of the three acute craniotomies to place up to three Neuropixels probes and the bipolar stimulating electrode. The schematic also shows two skull screws over the cerebellum that serve as the reference and the ground for the EEG signals. **(B)** Histological image of a coronal brain slice showing the location of the bipolar stimulating electrode (spanning MOs, layer 5; red dashed line) and one of the Neuropixels probes (spanning layers of MOs and anterior cingulate areas; blue dashed line) with fluorescent dyes (that appear red and green in the image). **(C)** Evoked responses from each of the 30 EEG electrodes from the awake, head-fixed mouse from -0.2 to +0.8 s following the electrical stimulus (vertical green line marks the onset time). Traces are arranged in the approximate orientation of the EEG array over the skull surface. Traces in black and gray represent signals that did and did not pass a quality control step, respectively. The red star and blue circles mark the approximate insertion point of the bipolar stimulating electrode and the Neuropixels probes, respectively. **Inset:** Single current pulses were biphasic (200 µs/phase), charge-balanced, and cathodic-first, with a current amplitude between 10-100 µA. **(D)** ERP (-0.2 to +0.8 s around stimulus onset) with all EEG electrode traces superimposed (butterfly plots). Each of the four panels represents data from a different stimulated area and depth: top and bottom left – superficial and deep layer (same as in panel C) MOs stimulation in the same subject; top and bottom right – superficial and deep layer SSp stimulation in a different subject. The dashed vertical line indicates the duration of the evoked signal; the marker above matches with the marker representing the value in panels **E** and **F**. The "baseline σ" indicates the standard deviation (in µV) over all electrodes during the 2 s preceding the stimulus. **(E)** Duration of the ERPs for all subjects based on the stimulation depth: superficial (N=12) vs. deep (N=18). **(F)** Normalized magnitude of the ERPs for all subjects based on the stimulation depth: superficial (N=12) vs. deep (N=18). For further details, see method "ERP duration and magnitude" and Figure 1-figure supplement 1. Boxplots show median (orange line), 25th, and 75th percentiles; whiskers extend from the box by 1.5x the inter-quartile range (IQR). * Weak evidence to reject null hypothesis ($0.05 > p > 0.01$), ** strong evidence to reject null hypothesis ($0.01 > p > 0.001$), *** very strong evidence to reject null hypothesis ($0.001 > p$).

The spiking response pattern of the stimulated cortex echoes the ERP

In addition to recording EEG signals, we simultaneously collected data from up to three Neuropixels probes – linear silicon probes with a 10 mm long non-tapered shank with 384 simultaneously recorded electrodes capable of capturing LFP and action potentials (Jun et al., 2017). The Neuropixels probes were placed in such a manner as to record from cortex (motor **MO**, anterior cingulate **ACA**, somatosensory **SS**, and visual **VIS**) and sensorimotor-related thalamic nuclei (**SM-TH**, Figure 2A), see full list of thalamic nuclei in the Methods section (Guo et al., 2017; J. A. Harris et al., 2019; Hooks et al., 2013). The Neuropixels probes were inserted approximately perpendicular to the cortical surface. This allowed us to observe the LFP and the spiking activity of hundreds of individual cortical and thalamic neurons. From the LFP, we infer the current source density (**CSD**) using a computational method that assumes an ohmic conductive medium, constant extracellular conductivity (0.3 S/m), and homogeneous in-plane neuronal activity, with the boundary condition of zero current outside the sampled area (Freeman & Nicholson, 1975; Mitzdorf, 1985).

We inserted a Neuropixels probe near the stimulating electrode (within 0.5 mm) and, often, up to two additional Neuropixels probes at distal locations. We observed direct responses (i.e., defined operationally as neurons that spike between 2-25 ms following the electrical pulse; this might miss a handful of very rapidly (i.e., < 2 ms) responding neurons; see Sombeck et al., 2022; Stoelzel et al., 2009) as well as indirect responses to the electrical stimulation. To look for cell-type specific activation patterns we classified regular spiking (**RS**) and fast spiking (**FS**) neurons (putative pyramidal and putative parvalbumin-positive inhibitory neurons, respectively) based on their spike waveform duration (RS duration > 4 ms; FS duration ≤ 0.4 ms) (Barthó et al., 2004; Bortone et al., 2014; Bruno & Simons, 2002; Jia et al., 2016; Niell & Stryker, 2008; Sirota et al., 2008).

Stimulating superficial MOs evoked a local spike, LFP and CSD response, followed by a period of quiescence lasting 94.2±16.1 ms in MO neurons (Figure 2C, left). There were minimal to no evoked responses (LFP, CSD, or spikes) in other sampled areas (Figure 2D-2F, left).

Stimulating deep MOs evoked a robust change in LFP and CSD, accompanied by spiking activity reflective of the two components in the ERP (Figure 2B right): an initial excitation within 25 ms (peak population firing rate 38.1±4.2 Hz), followed by quiescence (duration 125.0±5.5 ms) and a longer period of strong excitation (peak population firing rate 7.9±0.7 Hz; Figure 2C, right). This cortical response pattern was quite stereotyped – an initial excitation, followed by an off period and a strong rebound excitation – and was also observed in SM-TH (Figure 2F, right). We seldom observed this pattern for superficial stimulation (Figure 2C, left). Indeed, on average, about three times more cortical neurons respond significantly to deep than to superficial stimulation (Figure 4A and 4D).

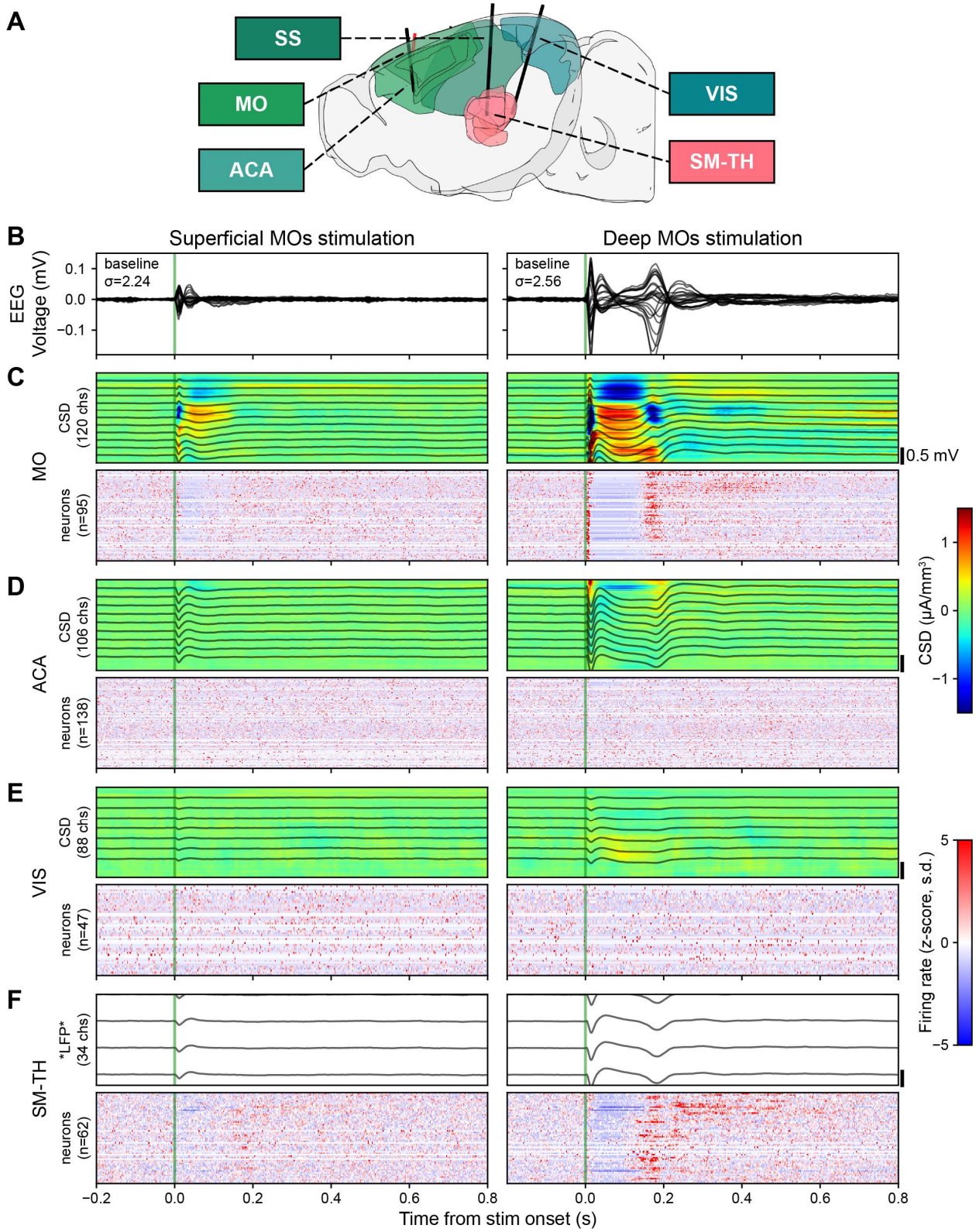
A
SS
MO
ACA
VIS
SM-TH
B
Superficial MOs stimulation
Deep MOs stimulation
EEG
Voltage (mV)
baseline
σ=2.24
baseline
σ=2.56
C
MO
CSD
(120 chs)
neurons
(n=95)
0.5 mV
D
ACA
CSD
(106 chs)
neurons
(n=138)
CSD (μA/mm³)
E
VIS
CSD
(88 chs)
neurons
(n=47)
Firing rate (z-score, s.d.)
F
SM-TH
LFP
(34 chs)
neurons
(n=62)
Time from stim onset (s)

Figure 2: Electrical stimulation evokes strong responses in the EEG, LFP, CSD, and in some populations of neurons (locally in motor cortex and in SM-TH) when deep layers of MOs are directly activated.

(A) Sagittal schema of the mouse brain, highlighting motor (MO), anterior cingulate (ACA), somatosensory (SS), visual (VIS), and somatomotor-related thalamic (SM-TH) areas (created using *brainrender*, Claudi et al., 2021). Solid black lines show the approximate locations of three acutely inserted Neuropixels probes; the red line indicates the stimulating electrode in the deep layers of MOs. **(B)** Butterfly plots of the ERP (-0.2 to +0.8 s around stimulus onset) evoked during the awake state. Each column represents data from a different stimulated depth (superficial and deep MOs) in the same subject (same subject shown in Figure 1D left top and bottom). **(C)** Evoked responses from the Neuropixels electrodes in MO. **Top:** From the measured LFP band (black traces representing 1 out of every 10 channels) the CSD response is computationally inferred (heat map, red and blue represent sources and sinks, respectively). The number of Neuropixels channels used to compute CSD is indicated along the y-axis. **Bottom:** Normalized firing rate, reported as a z-score of the average, pre-stimulus firing rate, of all neurons (only RS neurons in cortical regions) recorded by the Neuropixels probes targeting the area of interest. The number of neurons (n) in each area is included along the y-axis. **(D)** Evoked responses from the ACA, same as panel **C**. **(E)** Evoked responses from the VIS, same as panel **C**. **(F)** Evoked responses from the SM-TH, CSD was not computed for SM-TH because thalamic structures, unlike cortex, do not contain oriented neural elements (parallel axons) therefore it would not be interpretable.

Global ERPs are associated with widespread evoked cortical activity

Intrigued by the apparent lack of firing in non-stimulated cortical regions, we quantified the evoked magnitude of the LFP, CSD, and spiking in response to superficial and deep stimulation (note that our magnitude metric accounts for both reductions as well as increases and is calculated as the integral of the z-score relative to background; see method “LFP, CSD, and population spiking magnitude”; Figure 3A-3C). The magnitude of the LFP near the stimulation site is greater than background activity (54.0 s.d.·s in motor cortex) and decays with distance from the stimulation site (18.0 s.d.·s in visual cortex;

Figure 3A). Because the LFP reflects the summation of local presynaptic activity as well as volume conduction from more distant current sources (Kajikawa & Schroeder, 2011), we examined the CSD responses, which minimize the effect of volume conduction and emphasize local current flows. The magnitude of the CSD shows a similar pattern: large in stimulated cortex (51.4 s.d.·s in motor cortex) and smaller at more distant sites (4.8 s.d.·s in visual cortex), though the response is larger than baseline in both (Figure 3B). Yet while we see robust evoked firing of cortical neurons (30.9 s.d.·s in motor cortex) close to the stimulation electrode, changes in firing are often much smaller away from stimulation (1.8 s.d.·s in visual cortex; Figure 3C).

Stimulating superficial layers significantly modulated local LFP, CSD, and cortical spiking with respect to background (N=6; LFP median 19.8 [16.3-24.2 IQR], Wilcoxon signed-rank test corrected for multiple comparisons using Benjamini-Hochberg false discovery rate, p=0.0313; CSD 20.8 [17.5-22.9 IQR], p=0.0313; spiking 1.8 [0.5-5.0 IQR], p=0.0313; Figure 3D, left bars). It also modulated LFP and CSD in non-stimulated cortical areas (N=8; LFP 7.5 [5.1-9.7 IQR], p=0.0078; CSD 3.9 [2.7-10.0 IQR], p=0.0078), though to a lesser extent compared to the stimulated area. We did not detect evoked spiking outside of the stimulated area for superficial stimulation (-0.2 [-0.5-0.3 IQR], p=0.7422).

When we stimulated deep layers, we again observed large evoked LFP, CSD, and cortical spiking (deep, N=14; LFP 68.5 [55.3-79.2 IQR], Wilcoxon signed-rank test corrected for multiple comparisons using Benjamini-Hochberg false discovery rate, p=1.221E-4; CSD 95.1 [66.9-139.8 IQR], p=1.221E-4; spiking 29.3 [22.4-38.8 IQR], p=1.221E-4; Figure 3D, right bars). In contrast to superficial stimulation, deep stimulation-evoked responses in non-stimulated cortical regions were significantly greater than background (LFP 34.2 [18.5-51.3 IQR], p=3.052E-5; CSD 14.9 [11.9-33.4 IQR], p=3.052E-5, spiking 4.4 [2.7-10.1 IQR], p=3.052E-5).

Together, these data show that cortical stimulation evoked widespread changes in the LFP and CSD, but only evoked ipsilateral cortical spiking outside of the stimulated area when stimulating deep layers.

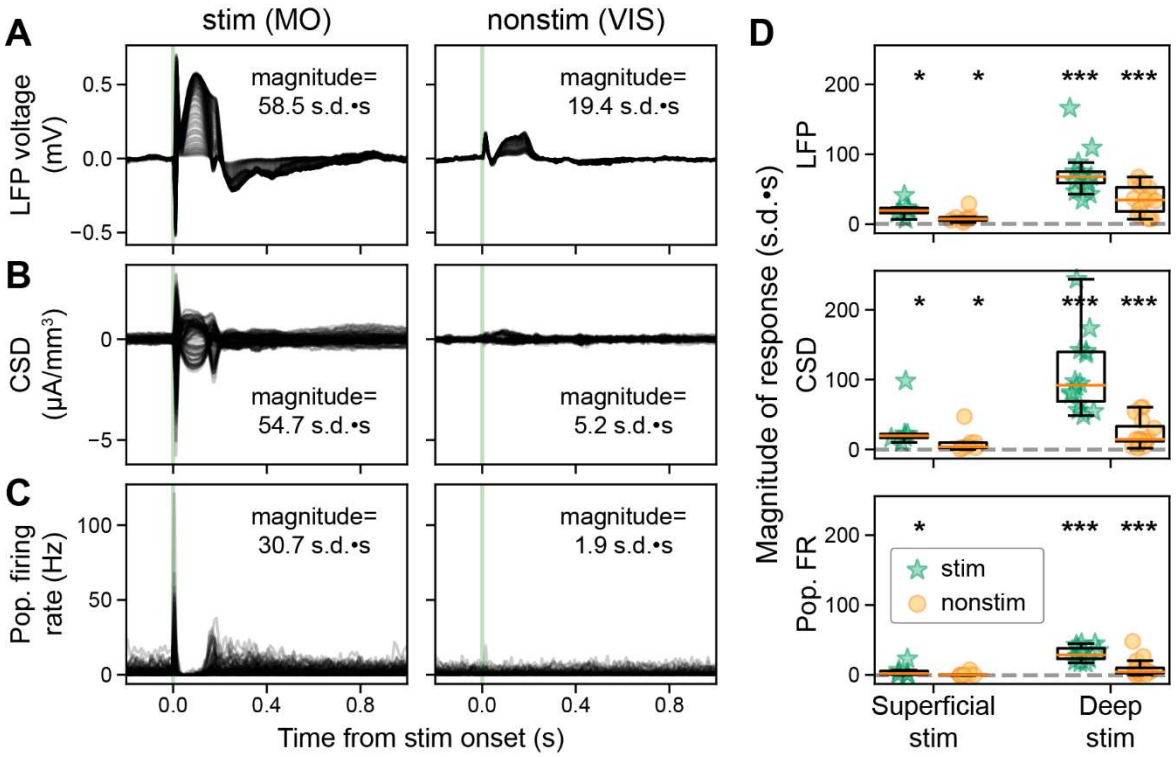

Figure 3: Direct stimulation of deep, but not superficial, cortical layers evokes widespread responses.

(A) Evoked LFP (-0.2 to +1.2 s around stimulus onset) from deep MOs stimulation (same subject as Figure 1D bottom left), all recorded cortical sites along the Neuropixels shaft are superimposed. The two columns represent data from stimulated (left) and a non-stimulated cortex (right). The magnitude is the integrated area of the response (0 to +0.5 s from stimulus onset), z-scored relative to the integrated area of the background activity calculated by shuffling the stimulation onset 1,000 times. **(B)** Evoked CSD from deep MOs stimulation, all recorded cortical sites along the Neuropixels shaft are superimposed. **(C)** Evoked neuronal firing rates from deep MOs stimulation, each trace represents a single RS neuron. **(D)** Magnitude of the evoked LFP (top), CSD (middle), and population spiking (bottom) to superficial (left) and deep stimulation (right) for stimulated and non-stimulated cortical regions (green stars and orange circles, respectively), dashed gray line at zero. Superficial stimulation: n=6

stimulated regions in N=6 mice and n=17 non-stimulated cortical regions in N=7 mice. Deep stimulation: n=15 stimulated regions in N=15 mice and n=35 non-stimulated cortical regions in N=16 mice. Boxplots show median (orange line), 25th, and 75th percentiles; whiskers extend from the box by 1.5x the IQR. Wilcoxon signed-rank test, corrected for multiple comparisons; * weak evidence to reject null hypothesis (0.05 > p > 0.01), ** strong evidence to reject null hypothesis (0.01 > p > 0.001), *** very strong evidence to reject null hypothesis (0.001 > p).

To further investigate the evoked neural spiking across both stimulated and non-stimulated areas, we computed the percentage of modulated (significantly increased or decreased spiking relative to the pre-stimulus baseline) RS neurons per subject in three temporal windows following the stimulus: 2-25 ms (initial excitation), 25-150 ms (off period), and 150-300 ms (rebound excitation; Figure 4). The three temporal windows were chosen to match the stereotyped firing patterns, which align with maximum peaks in the ERPs and the period in between (Figure 1-figure supplement 2). We separately analyzed FS neurons and found they behave like RS neurons (Figure 4-figure supplement 1); therefore, further analyses focus only on RS neurons.

During the initial excitation, the fraction of activated (significantly increased spiking relative to baseline) neurons was always higher in the stimulated cortex than other cortical areas, for both superficial and deep stimulation. The fraction of activated neurons in non-stimulated ipsilateral cortical regions was only marginally above zero (Figure 4A and 4D). Indeed, across all 24 animals, only an average of 0.5% (minimum 0%, maximum 2.6%) of the neurons were modulated in the initial excitation, compared to an average of 17.8% (minimum 0%, maximum 83.3%) in stimulated cortex.

Next, we quantified the fraction of modulated RS neurons in the off period between 25 and 150 ms, capturing the period between the two large ERP amplitude components (present with deep stimulation; Figure 1-figure supplement 2). There were very few neurons with increased spiking, regardless of

stimulation depth and area (mean 0.4%, minimum 0%, maximum 2.8%; Figure 4B and 4E). In contrast, spiking in 18/22 subjects was significantly reduced from baseline following either superficial or deep stimulation. Interestingly, some non-stimulated areas showed decreased spiking but only in response to deep stimulation (mean 10.1%, minimum 0%, maximum 55.7%).

The final temporal window we considered was the rebound excitation window between 150 and 300 ms, coinciding with the second component in the ERP. All 16 subjects who received deep stimulation showed significant rebound excitation in the stimulated cortex, whereas only 1/6 superficial stimulation subjects did (Figure 4C and 4F). Some subjects who received deep stimulation showed significant rebound excitation in the non-stimulated areas (6/16; Figure 4F), but it was nonexistent amongst the superficial stimulation subjects (0/7; Figure 4C).

To summarize, deep cortical stimulation is more likely to significantly modulate single neurons outside of the stimulated cortical area. This largely consisted of decreases in firing in the 25-150 ms window and mixed increases and decreases in firing during the 150-300 ms window (Figure 4F).

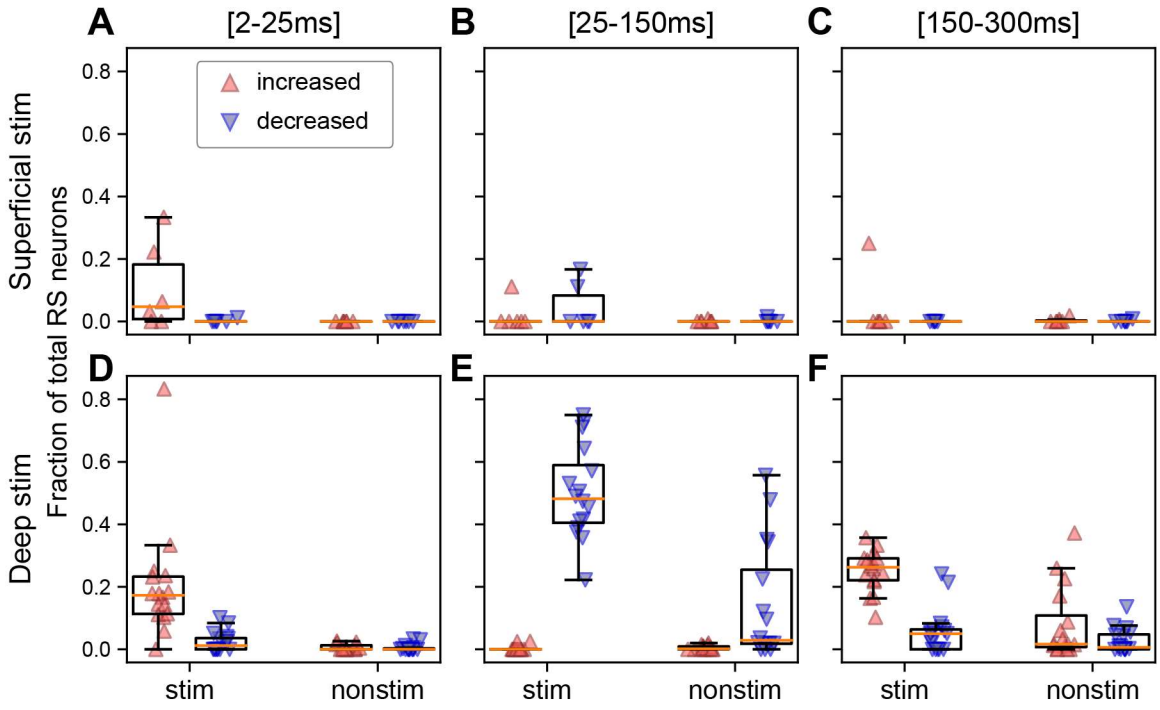

Figure 4: The fraction of the neuron population per ipsilateral cortical area in each subject that is significantly modulated depends on the depth of stimulation and the temporal window.

(A) Fraction of RS neurons per cortical area in each subject that exhibit a significantly increased (red upward triangle) or decreased (blue downward triangle) response in the first 25 ms for superficial stimulation. Fraction of RS neurons that exhibit a significant increase or decrease **(B)** 25-150 ms or **(C)** 150-300 m following the stimulus. **(D-F)** Same as panels **A-C** but for deep stimulation. Panels **A-C** are derived from 870 RS neurons from stimulated cortex and 4,110 RS neurons from non-stimulated cortical regions in N=7 mice and panels **D-F** from 2,559 RS neurons from stimulated cortex and 9,363 RS neurons from non-stimulated cortical regions in N=17 mice. Boxplots show median (orange line), 25th, and 75th percentiles; whiskers extend from the box by 1.5x the IQR.

Cortico-thalamo-cortical interactions underlie features of the ERPs

The striking tri-phasic cortical spiking pattern for deep stimulation is replicated in the associated thalamic nuclei that are connected to the stimulated cortical area (here SM-TH; Guo et al., 2017; Harris

et al., 2019; Hooks et al., 2013; bottom right in Figure 2F), though shifted in time. Specifically, we observed a brief excitation (peak population firing rate 22.3±3.2 Hz), a 74.6±15.5 ms long period of suppression, followed by rebound excitation (peak population firing rate 14.7±1.0 Hz). This is not the case when stimulating superficial layers (Figure 2F, bottom left).

We quantified the fraction of significantly modulated neurons in the SM-TH population and found that the neurons were almost eight times more likely to be modulated by deep than superficial stimulation (superficial: 5.0±4.1% of SM-TH population, N=5; deep: 37.9±20.6%, N=14; Student's two-tailed t-test, p=0.0037; Figure 5A).

Thalamic response shows bursts of action potentials during the rebound (Figure 5B and 5D); bursting is a well-known activity mode of thalamic relay cells and is defined as two or more consecutive spikes with an inter-spike interval less than 4 ms preceded by at least 100 ms of silence (Contreras & Steriade, 1995; Grenier et al., 1998; Guido & Weyand, 1995; Halassa et al., 2011; Lu et al., 1992; Nestvogel & McCormick, 2021). We quantified the average burst probability (75-300 ms after stimulus onset) and found that deep stimulation had a significantly higher likelihood of evoking bursts (superficial stimulation: median 0 [0-0.02 IQR]; deep stimulation: median 0.12 [0.02-0.2 IQR]; Mann-Whitney *U* test, p=0.0258; Figure 5C).

We hypothesized that deep stimulation elicits spiking in cortico-thalamic projection neurons, followed – with some delay due to axonal propagation and synaptic transmission – by thalamic neurons, whereas during the rebound period thalamic bursting precedes cortical rebound spiking (Figure 5B and 5D). Indeed, during the initial excitation, stimulated cortical RS cells had a median first-spike latency of 4.4±0.9 ms, with the thalamic population following at 11.4±2.8 ms (mean latency difference of 6.9 ms; paired t-test, p=4.838E-6; Figure 5E). During the rebound excitation window, the temporal relationship

flipped: the thalamic population had a median rebound spike latency of 148.2±21.2 ms, with cortex following at 184.2±17.3 ms (mean latency difference -36.0 ms; paired t-test, p=2.136E-4; Figure 5F).

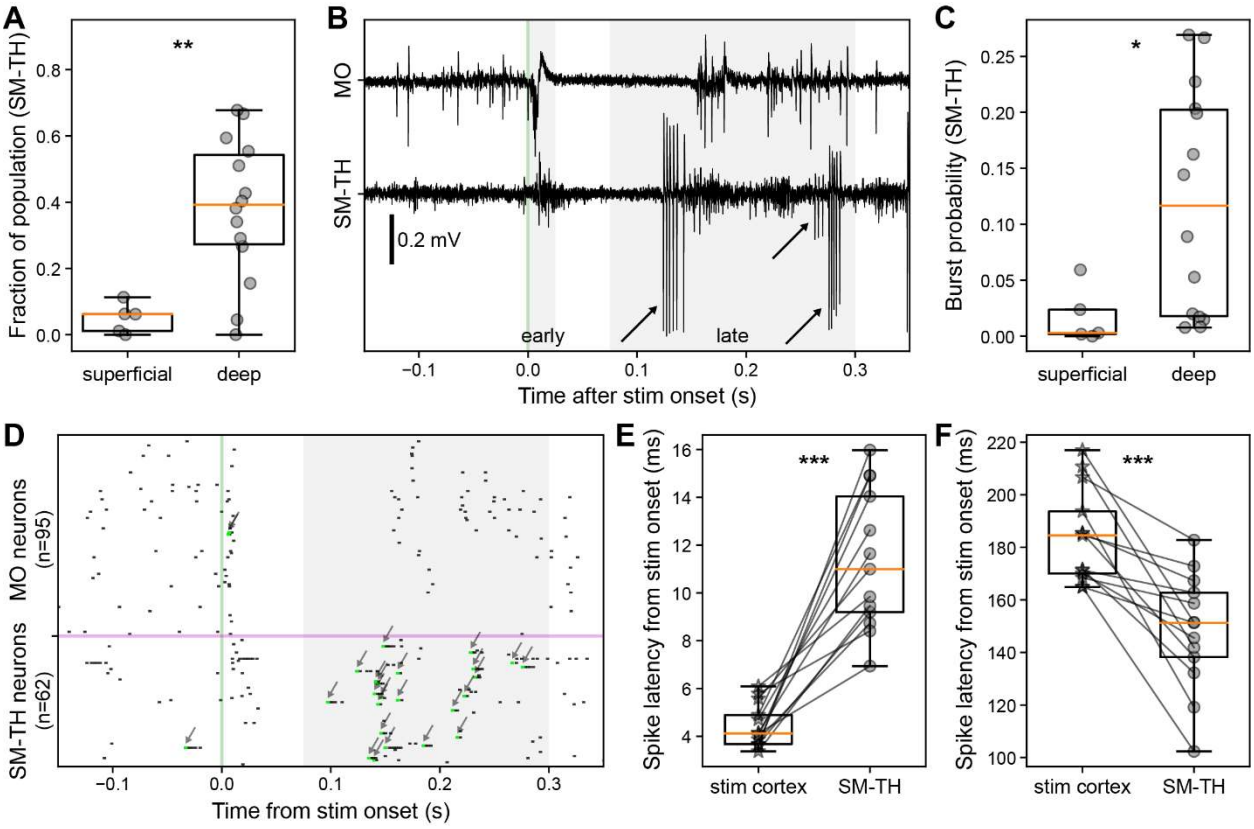

Figure 5: Cortical and thalamic neural dynamics evoked by cortical electrical stimulation.

(A) Fraction of SM-TH neurons that exhibit a significant increase or decrease in firing rate compared to baseline between 2 ms and 300 ms following stimulus onset for superficial (N=5) and deep stimulation (N=14). **(B)** Raw traces from the Neuropixels spike band data for MO (top) and SM-TH (bottom; -0.15 to +0.35 s) for one exemplar trial with deep MOs stimulation. Action potential bursts in the SM-TH are flagged with arrows. **(C)** Probability (fraction of total trials) that the SM-TH produces bursts within 75-300 ms from stimulus onset for superficial (N=5) and deep stimulation (N=14). **(D)** Single trial raster plot showing spiking of MO (top) and SM-TH neurons (bottom) in response to a single deep electrical pulse (at the green vertical line). Action potential bursts are flagged with arrows. **(E)** Latency to first-spike (2-25 ms) for responsive RS neurons in stimulated cortex (stars) and in associated

SM-TH (circles). Populations are recorded simultaneously in each subject, represented by the connecting black lines (N=13). **(F)** Latency to spike in the late window (75-300 ms) for responsive RS neurons in stimulated cortex (stars) and in SM-TH (circles), as in panel **E**. Boxplots show median (orange line), 25th, and 75th percentiles; whiskers extend from the box by 1.5x the IQR. * Weak evidence to reject null hypothesis (0.05 > p > 0.01), ** strong evidence to reject null hypothesis (0.01 > p > 0.001), *** very strong evidence to reject null hypothesis (0.001 > p).

Similarly, the CSD analysis generated results supporting our initial hypothesis. Thalamic bursts powerfully activate cortical neurons (Borden et al., 2022; Nestvogel & McCormick, 2021; Ramcharan et al., 2005; Sherman, 1996) via synaptic activity that can be captured by the inferred CSD. We observed a pronounced current sink near the border of layers 2/3 and 5 in MOs (near the deep stimulation site) that coincided with the timing of the thalamic rebound burst (~180 ms). This was consistent across subjects (N=9, Wilcoxon signed-rank test, p<0.05; Figure 6A). We also analyzed the correlation between the ERP and laminar CSD on a trial-by-trial basis and found that the EEG signals correlated more strongly with CSD of deep compared to superficial layers (Figure 6-figure supplement 1). To further investigate the relationship between thalamic bursting, cortical spiking, and the ERP, we computed the correlation between these metrics in the rebound window (75-300 ms after stimulus onset) on a trial-by-trial basis for each subject. The fraction of bursting SM-TH neurons was correlated with the cortical population firing rate (8/13 mice with a significant correlation [p<0.05], mean Pearson r value: 0.4±0.04; Figure 6B). The cortical population firing rate was likewise correlated with the magnitude of the second, late component in the ERP (9/13 mice with a significant correlation [p<0.05], mean Pearson r value: 0.5±0.04; Figure 6C). Additionally, the late component in the ERP was significantly correlated with the fraction of bursting SM-TH neurons (13/13 mice with a significant correlation [p<0.05], mean Pearson r value: 0.5±0.07; Figure 6-figure supplement 2A), much more so than it was correlated with the SM-TH

population firing rate (Figure 6-figure supplement 2B). These important observations link micro-scale dynamics (cellular thalamic bursting) with a macro-scale read-out (cortical EEG).

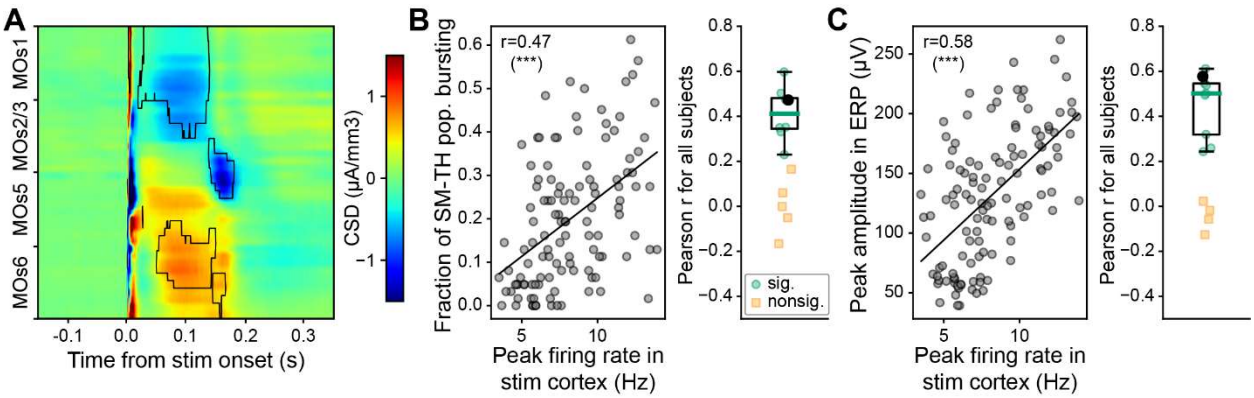

Figure 6: Thalamic origins of the late ERP component.

(A) Population level (N=9) CSD analysis of MOs after deep MOs stimulation (sinks blue, sources red). The black traces outline the areas with significant and consistent responses across subjects (Wilcoxon signed-rank test, p<0.05). **(B) Left:** Pearson correlation between fraction of SM-TH neurons that burst and peak cortical population firing rate on a trial-by-trial basis for one mouse (same subject as in Figure 1D bottom left). **Right:** Same as left, computed for all (N=13) mice with deep stimulation; the black circle represents the subject from the left panel, green circles represent subjects with a significant correlation (p<0.05), and yellow squares represent subjects with a non-significant correlation. **(C) Left:** Pearson correlation between peak amplitude of the second, late component in the ERP and peak cortical population firing rate on a trial-by-trial basis for one example mouse (as in panel **B**). **Right:** Same as left, computed for all subjects with deep stimulation (N=13), represented as in panel **B**. Boxplots show median (green line), 25th, and 75th percentiles; whiskers extend from the box by 1.5x the IQR. * Weak evidence to reject null hypothesis (0.05 > p > 0.01), ** strong evidence to reject null hypothesis (0.01 > p > 0.001), *** very strong evidence to reject null hypothesis (0.001 > p).

Behavioral states modulate the ERP and the cortico-thalamic interactions

To study differences between the evoked responses across conscious and unconscious states, we performed experiments on mice that were awake and subsequently anesthetized. At the start of an experiment, we delivered up to 120 single electrical pulses while the mouse was awake, free to rest or run on a freely moving wheel. Next, we induced anesthesia with isoflurane via inhalation. Once the mouse reached a stable level of unconsciousness (no reaction to an alcohol swab placed in front of the nose; 4.0±0.3 min after induction onset at 5% isoflurane concentration), we delivered the same set of electrical stimuli.

We separated each trial by behavioral state based on whether the animal was stationary (*quiet wakefulness*) or running (*active wakefulness*, defined here as an average running speed exceeding 0 cm/s in a window from -0.5 to 0.5 s from the stimulation onset). We then compared average responses from 97 (median, [86-104 IQR]) quiet wakefulness, 21 (median, [16-27 IQR]) active wakefulness, and 120 (median, [120-120 IQR]) anesthetized trials across 17 animals. Both locomotion and anesthesia visibly modulated the ERPs (Figure 7A) and the evoked firing rates of cortical and thalamic neurons (Figure 7B). The second component in the ERP is diminished when running and nonexistent during anesthesia; this is captured by the decrease in ERP duration (quiet wakefulness 0.5±0.1 s, running 0.3±0.0 s, anesthetized 0.3±0.0 s; Friedman test, state effect: Q(2)=15.6, p=4.002E-4; Figure 7C) and the decrease in ERP magnitude (quiet wakefulness 6.1±0.9, running 1.6±0.3, anesthetized 1.6±0.3; Friedman test, state effect: Q(2)=17.4, p=1.656E-4; Figure 7D).

Next, we examined how cortical and thalamic activity differed as a function of behavioral state. In both regions, the baseline firing rates (measured during the pre-stimulus epoch) were higher during running and lower during anesthesia compared to quiet wakefulness (stimulated cortex baseline firing rate: N=16, quiet wakefulness 3.5±0.2 Hz, running 5.2±0.5 Hz, anesthetized 1.1±0.2 Hz; one-way repeated

measures (RM) ANOVA, state effect: F(2, 30)=66.3, p=2.901E-9, Figure 7E left; SM-TH baseline firing rate: N=13, quiet wakefulness 9.0±1.4 Hz, running 16.4±1.5 Hz, anesthetized 0.8±0.4 Hz; Friedman test, state effect: Q(2)=24.2, p=5.689E-6, Figure 7E right).

The median first spike latencies for cortical and thalamic populations were the same when looking at the initial excitation (N=13; stimulated cortex latency: quiet wakefulness 4.5±0.3 ms, running 4.0±0.2 ms, anesthetized 4.6±0.4 ms; SM-TH latency: quiet wakefulness 11.5±0.8 ms, running 11.3±0.8 ms, anesthetized 10.9±0.6 ms; two-way RM ANOVA, state effect: F(2, 24)=0.3, p=0.6281, region effect: F(1, 12)=89.3, p=6.581E-7, interaction: F(2, 24)=0.5, p=0.5062; Figure 7F). However, the rebound spike latencies for cortex and thalamus were earlier during running compared to quiet wakefulness (N=13; stimulated cortex latency: quiet wakefulness 186.7±4.6 ms, running 163.8±5.0 ms, anesthetized 200.2±7.5 ms; SM-TH latency: quiet wakefulness 156.0±7.1 ms, running 123.1±3.9 ms, anesthetized 195.1±9.5 ms; two-way RM ANOVA, state effect: F(2, 24)=31.4, p=2.020E-7, region effect: F(1, 12)=17.2, p=1.349E-3, interaction: F(2, 24)=6.6, p=0.053; Figure 7G). The cortex and thalamus did not exhibit consistently timed rebound excitation during anesthesia, so the relative timing during this state was random and often later than during quiet and active wakefulness. The probability of evoking thalamic bursts decreased during running compared to quiet wakefulness and was very low (zero for many subjects) during anesthesia (N=13; median probability: quiet wakefulness 0.1 [0.01-0.24 IQR], running 0 [0-0.07 IQR], anesthetized 0 [0-0.002 IQR]; Friedman test, state effect: Q(2)=18.6, p=9.142E-5; Figure 7H).

Thus, thalamic activity preceded cortical activity during the rebound excitation in both quiet and active wakefulness. However, during quiet wakefulness the rebound is characterized by thalamic burst firing, which correlated with increased cortical spiking and higher ERP magnitudes (Figure 6).

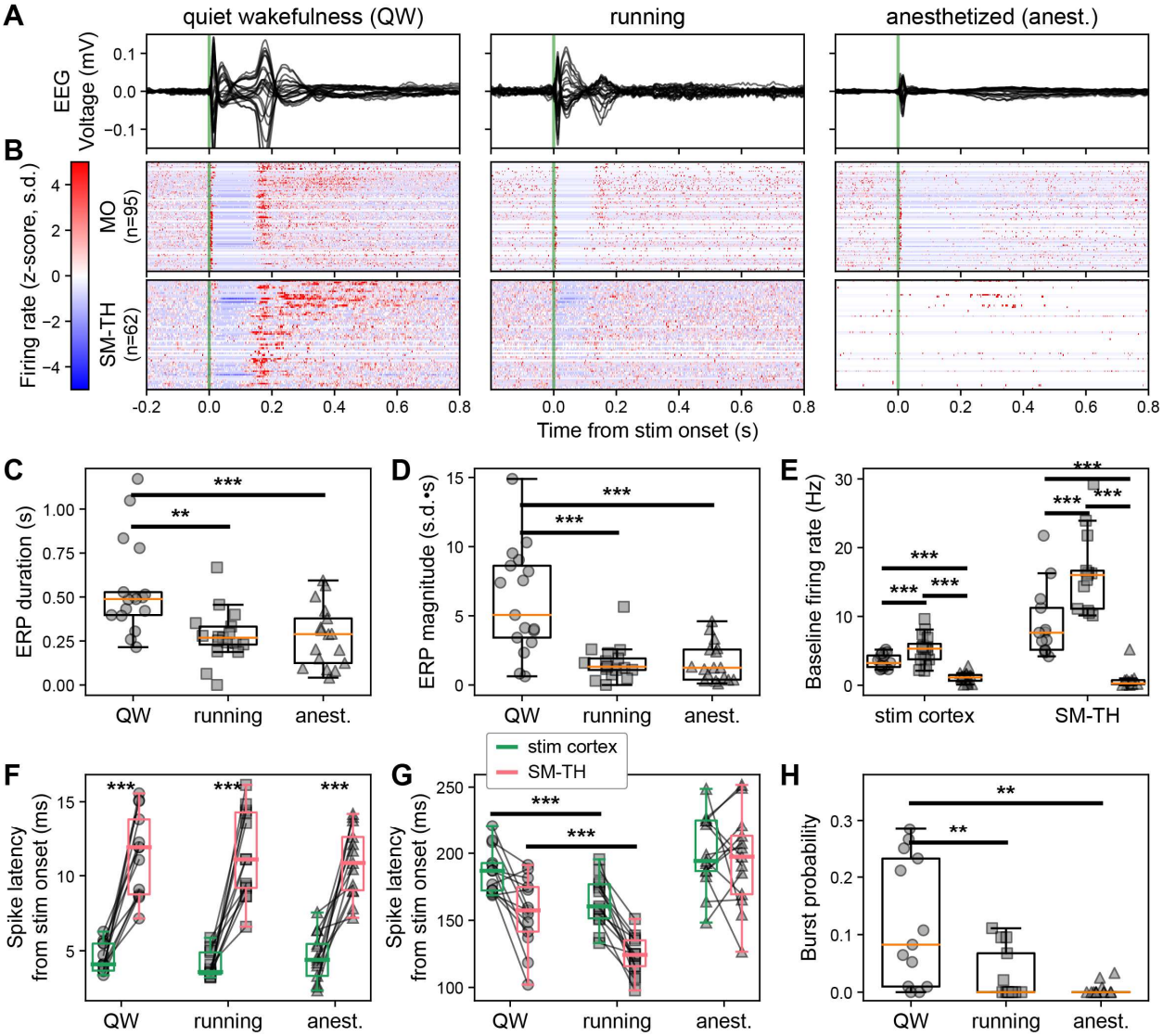

Figure 7: Brain state modulates the ERP via cortico-thalamo-cortical interactions.

(A) Butterfly plot of ERPs during non-running (quiet wakefulness), running (active wakefulness) and isoflurane-anesthetized states (same subject as in Figure 1D bottom left). **(B)** Normalized firing rate, reported as a z-score of the average, pre-stimulus firing rate, of all RS neurons recorded by the Neuropixels probes targeting the stimulated cortex (MO) and SM-TH. **(C)** Duration and **(D)** magnitude of the ERPs for all states (see also Figure 1E,F): quiet wakefulness, running, and anesthetized (N=17). **(E)** Baseline rates of cortical (stim cortex) and SM-TH neurons across all states (stim cortex: N=16; SM-TH: N=13). Latency to first-spike in **(F)** early (2-25 ms) and **(G)** late (100-300 ms) windows for responsive RS neurons in the stimulated cortex (green boxes) and in the SM-TH (pink boxes)

across all states. Populations are recorded simultaneously in each subject, represented by the connecting black lines (N=12). **(H)** Probability (fraction of total trials) of SM-TH spiking bursts within 75-300 ms from the stimulus onset for the three states (N=13). Boxplots show median, 25th, and 75th percentiles; whiskers extend from the box by 1.5x the IQR. * Weak evidence to reject null hypothesis (0.05 > p > 0.01), ** strong evidence to reject null hypothesis (0.01 > p > 0.001), *** very strong evidence to reject null hypothesis (0.001 > p).

Thalamo-cortical interactions affect perturbational complexity in head-fixed mice

The differences of ERPs across behavioral states, reflecting differences in the cortico-cortical and cortico-thalamic interactions as described above, resulted in significant changes in complexity across states (Figure 8A). To quantify complexity, we used an algorithm that quantifies the number of state transitions for each principal component in the ERP (**PCIST**; Comolatti et al., 2019). Like the PCI, this metric distinguishes conscious from unconscious states in a variety of human volunteers and patients with disorders of consciousness (Comolatti et al., 2019) as well as rodents (Arena et al., 2021; Cavelli et al., 2022); unlike PCI, PCIST does not require source modeling and is not upper-bounded by 1. When PCIST is high, signals are both spatially and temporally differentiated. When it is low, signals are highly correlated across space and time or very small relative to the pre-stimulus signal. We found that PCIST was higher during the awake state than during the isoflurane-anesthetized state in all subjects (N=31; awake PCIST 45.5±3.6; anesthetized PCIST 16.5±2.4; paired t-test, p=2.508E-11; Figure 8B).

Based on our observation that superficial stimulation evoked simpler responses than deep stimulation (in the awake state), we found that PCIST was, indeed, significantly lower for superficial than for deep stimulation (superficial: N=13, awake PCIST 35.6±4.8; deep: N=18, awake PCIST 52.7±4.4; Student's two-tailed t-test, p=0.0179; Figure 8C).

To compare PCI^{ST} during quiet and active wakefulness, and isoflurane anesthesia, we selected subjects that had at least 30 running trials (for this comparison, trial numbers were matched within subject, on average 51 trials) since averaging the ERP over too few trials can affect the PCI^{ST} calculation. Comolatti et al. (2019) showed that PCI^{ST} increased as the number of trials increased, specifically in wakefulness because averaging over more trials increases the signal-to-noise ratio of the ERP by reducing the contribution of background, non-stimulus-evoked activity. PCI^{ST} was significantly different for all states; the highest complexity ERPs were seen when mice were in quiet wakefulness, slightly lower complexity ERPs during active wakefulness, with the lowest complexity during anesthesia (N=8; quiet PCI^{ST} 55.2±10.3, active wakefulness 39.9±7.7; anesthetized 14.0±5.8; one-way RM ANOVA, state effect: $F(2, 14)=28.3$, $p=1.202E-5$; Figure 8D).

To test whether PCI^{ST} recovered to baseline after anesthesia, we repeated the same set of 120 electrical stimuli up to two times over one hour following cessation of the isoflurane in a subset of mice. All but one subject showed an increase in PCI^{ST} (reaching pre-anesthesia levels) in the first 30 minutes after cessation of isoflurane, but the complexity did not increase further in the subsequent 30 minutes (N=13; awake PCI^{ST} 48.0±4.0; anesthetized PCI^{ST} 14.3±2.3; recovery 0-30 minutes PCI^{ST} 32.7±4.9; recovery 30-60 minutes PCI^{ST} 36.4±5.0; RM ANOVA, state effect: $F(3, 18)=11.6$, $p=1.804E-4$; Figure 8E).

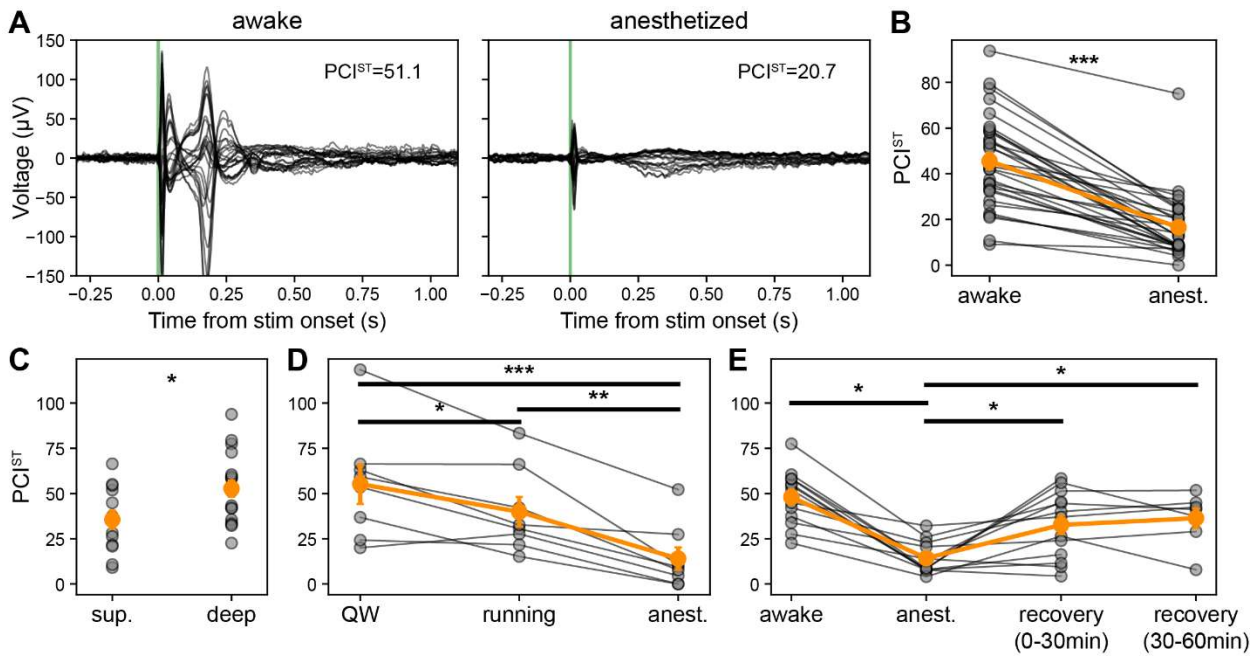

Figure 8: Perturbational complexity is modulated by cortico-thalamo-cortical interactions.

(A) Butterfly plot of ERP (-0.3 to +1.1 s) from awake (left) and anesthetized states (right). Same subject as in Figure 1D bottom left, annotated with PCI^{ST} values. **(B)** PCI^{ST} calculated using EEG evoked responses (baseline -0.8 to -0.002 s and response 0.002 to 0.8 s) for awake and anesthetized states. Individual values represented with gray connected circles (N=31 sessions across 24 mice). **(C)** PCI^{ST} for superficial versus deep cortical stimulation while mice are awake (includes quiet wakefulness and running trials). **(D)** PCI^{ST} for quiet wakefulness, running, and anesthetized states. Individual values represented with gray connected circles (N=8). **(E)** PCI^{ST} for quiet wakefulness, anesthetized, and two subsequent recovery states. Individual values represented with gray connected circles (N=13). Orange circles and error bars represent mean ± SEM. * Weak evidence to reject null hypothesis (0.05 > p > 0.01), ** strong evidence to reject null hypothesis (0.01 > p > 0.001), *** very strong evidence to reject null hypothesis (0.001 > p).

DISCUSSION

We recorded brain-wide, multi-scale, evoked EEG, LFP, and single neuron responses to cortical electrical stimulation in head-fixed mice that are awake and, subsequently, anesthetized with isoflurane. We find that cortico-thalamo-cortical (**CTC**) interactions drive the long-lasting ERPs elicited by deep cortical stimulation during quiet wakefulness. The thalamic rebound response is characterized by thalamic burst firing that temporally coincides and is correlated with the second, late component in the ERP. Furthermore, the CTC interactions are modulated by the behavioral state of the animal, which is mirrored in the ERP.

Electrically evoked spiking pattern depends on the depth of stimulation

Electrical stimulation of superficial layers results in a brief excitation followed by 44.3±16.4 ms of silence in local cortical neurons only (without any detected involvement of the thalamus). This pattern has been seen in different species (Butovas et al., 2006; Butovas & Schwarz, 2003; Cavelli et al., 2022; Chung & Ferster, 1998; Contreras & Steriade, 1995; Douglas & Martin, 1991; Grenier et al., 1998; Hao et al., 2016; Kara et al., 2002; Logothetis et al., 2010; Sombeck et al., 2022; Vyazovskiy et al., 2013) and is reminiscent of the bi-stability (a state characterized by spontaneous alternation between bouts of activity and periods of silence) reported in deep sleep and in unconscious patients following a brief stimulation (Hill & Tononi, 2005; Pigorini et al., 2015; Rosanova et al., 2018; Timofeev et al., 2001; Usami et al., 2015).

Deep electrical stimulation elicits a stereotyped tri-phasic spiking pattern – a brief excitation followed by 127.8±4.1 ms of silence and a *rebound* excitation – in local cortical and thalamic neurons. Other studies also describe rebound excitation at similar latencies following stimulation-evoked quiescent periods (Butovas et al., 2006; Butovas & Schwarz, 2003; Cavelli et al., 2022; Grenier et al., 1998). This local, cortical down-state may be due to a brief shift in excitatory-inhibitory balance, a large fraction of

cortical cells being refractory, and/or a lack of excitatory input from the thalamus. We see similar response profiles in both RS and FS cells (Figures 2, 4, and S3).

Given the direct projections from deep pyramidal neurons to thalamic regions (J. A. Harris et al., 2019; K. D. Harris & Shepherd, 2015; Hooks et al., 2013), it is not surprising that we observe strong recruitment of thalamic neurons 6.7 ms (on average) following the onset of cortical spiking. The thalamic spiking pattern evoked by deep stimulation during quiet wakefulness – brief excitation followed by a period of quiescence (74.6±15.5 ms) and a subsequent burst of action potentials – is consistent with previously described thalamic responses to cortical stimulation (Contreras & Steriade, 1995; Grenier et al., 1998). The fast action potential bursts in thalamic cells following the period of quiescence are likely to be triggered by low-threshold Ca^{2+} spikes, known to follow periods of pronounced hyperpolarization in thalamic relay neurons (Borden et al., 2022; Contreras & Steriade, 1995; Grenier et al., 1998; Guido & Weyand, 1995; Halassa et al., 2011; Lu et al., 1992; Nestvogel & McCormick, 2021; Urbain et al., 2019). The thalamic silence-burst pattern may be a result of a withdrawal of excitation due to the cortical down-state or disynaptic inhibition via stimulation of thalamic reticular neurons, a primary source of GABAergic input to the thalamus (Bal et al., 2000; Domich et al., 1986; Pinault, 2004; Sherman & Guillery, 1996), both leading to the low-threshold Ca^{2+} spike burst. We are currently unable to distinguish between these two possible mechanisms but are planning follow-up experiments to address this important question.

Evoked thalamic bursting consistently preceded cortical rebound spiking by 37.0 ms (on average, Figure 5F), comparable to the latency described by Grenier et al. (1998). The occurrence of bursts is compatible with these being thalamic relay neurons that excite their cortical targets (Guo et al., 2017; Sherman, 2001). Numerous previous studies have shown that thalamic relay neurons exhibit *spontaneous* bursting during anesthesia (Contreras & Steriade, 1995; Grenier et al., 1998; Swadlow & Gusev, 2001), NREM

sleep (Domich et al., 1986; Halassa et al., 2011; Urbain et al., 2019), drowsiness (Stoelzel et al., 2009; Swadlow & Gusev, 2001), and wakefulness (Nestvogel & McCormick, 2021; Urbain et al., 2015). In our hands, thalamic relay neurons exhibit *evoked* rebound bursting during quiet wakefulness, but not during running or isoflurane anesthesia. This is consistent with findings showing that thalamic hyperpolarization and low-threshold Ca^{2+} spike-bursting coincides with movement offset in mice (Nestvogel & McCormick, 2021). Likewise, some anesthetics decrease the probability of thalamic bursts; specifically, isoflurane has been shown to shunt the low-threshold Ca^{2+} spikes and, therefore, the associated bursting (Ries & Puil, 1999; this does not rule out additional cortical effects of isoflurane, e.g., Bharioke et al., 2022). Therefore, our finding does not contradict results from other studies reporting evoked thalamic bursting in unconscious states, such as anesthesia via pentobarbital or ketamine/xylazine (Contreras & Steriade, 1995; Grenier et al., 1998) and NREM sleep (Urbain et al., 2019), which are likely to affect thalamic neurons in different ways compared to isoflurane.

Thalamo-cortical dynamics modulate perturbational complexity in mice

The behavioral state of the mouse strongly affects the underlying neural activity (Figure 7). Running and isoflurane anesthesia modulates the excitability of the network in opposing directions. Cortical firing rates during quiet wakefulness, 3.3±0.2 Hz, increase to 5.0±0.5 Hz for active wakefulness and decrease to 1.1±0.2 Hz during anesthesia (Figure 7E left); likewise in SM-TH, where baseline rates increase from 9.4±1.5 Hz during quiet wakefulness to 16.8±1.6 Hz during active wakefulness and drop to 0.8±0.4 Hz during anesthesia (Figure 7E right). Conversely, the median probability of electrically evoked thalamic bursting decreases from its baseline during quiet wakefulness of 9.5% ([10.0-23.7 IQR] to effectively zero for both active wakefulness [0-7.4 IQR] and anesthesia [0-0.2 IQR]). While we cannot conclusively rule out that mice were asleep during the *quiet wakefulness* periods we analyzed, we believe they are likely to be awake because the experiments are performed during the dark phase of the light/dark cycle, when

they are less likely to enter a sleep state (Franken et al., 1999) and the mice do not undergo specific training to promote drowsiness or sleep.

The stimulus-evoked bursts in the thalamus and the resulting thalamo-cortical interaction, that primarily occur when the animal is in quiet wakefulness, result in longer, higher amplitude ERPs (Figure 7C and 7D). This is consistent with previous studies showing that stimulus-evoked bursting in thalamic relay neurons robustly activates cortical neurons (Borden et al., 2022; Nestvogel & McCormick, 2021; Ramcharan et al., 2005; Stoelzel et al., 2009; Swadlow & Gusev, 2001), with a cortical rebound depolarization lasting up to ~0.5 s (Grenier et al., 1998), and 3-5 Hz cortical oscillation of ~1 s median duration (Nestvogel & McCormick, 2021). Indeed, the more thalamic cells burst during the rebound period, the larger the magnitude of the second, late component in the ERP (Figure 6-figure supplement 2A). This observed link between the ERP and activity in the CTC loop, an important finding made possible by our unique experimental design, may help interpret the complex physiological and behavioral effects of electrical or magnetic stimulation on the human brain (Borchers et al., 2011).

ERPs are associated with higher PCI^{ST} values during awake than during isoflurane anesthesia (quiet wakefulness PCI^{ST} 55.2±10.3; active wakefulness PCI^{ST} 39.9±7.7; anesthetized PCI^{ST} 14.0±5.8), consistent with prior work in humans (Comolatti et al., 2019) and in rodents (Arena et al., 2021; Cavelli et al., 2022). Furthermore, the ERPs are shorter and the associated PCI^{ST} lower during active wakefulness than during quiet wakefulness, possibly due to a lower probability of evoked thalamic bursting. All subjects have higher PCI^{ST} during active wakefulness compared to anesthesia (active wakefulness PCI^{ST} 39.9±7.7; anesthetized PCI^{ST} 14.0±5.8). The comparison of PCI^{ST} across quiet wakefulness, active wakefulness, and anesthesia suggests that in mice there is an optimal network state which maximizes complexity, reminiscent of the inverted-U relationship between arousal and task performance (McGinley et al., 2015; Yerkes & Dodson, 1908).

The last decade has witnessed the emergence of the mouse as a model organism to study the neuronal correlates of consciousness (Aru et al., 2020; Bharioke et al., 2022; Koch et al., 2016; Larkum, 2013; Sachidhanandam et al., 2013; Suzuki & Larkum, 2020). These studies point to the critical role of layer 5 pyramidal neurons, as well as cortico-cortical feedback to apical dendrites of infragranular pyramidal neurons. Although the present study was not designed with a classical perceived vs. non-perceived paradigm in mind (Koch et al., 2016), our finding of shorter and less complex ERPs and a reduced effectiveness of the CTC circuit during isoflurane anesthesia is certainly compatible with such results. To understand the extent to which our results generalize, it would be important to apply the PCI method to a diversity of different anesthetics in mice (e.g., Arena et al., 2021; Bharioke et al., 2022; Cavelli et al., 2022) and investigate the role of thalamic bursting and CTC activity in relation to large scale EEG dynamics in such states.

Thalamic-mediated local neural responses underlie global ERP in distant cortical regions

Based on the presence of dense intercortical connections between areas (from neurons in layers 2/3-6; J. A. Harris et al., 2019), we expected that cortical stimulation during quiet wakefulness would directly elicit synaptic and spiking activity in other cortical sites outside the stimulated area. We observed large-amplitude evoked activity in the EEG and LFP in ipsilateral cortical regions close (0.5-1 mm) and up to 5 mm away from the stimulated site (Figures 2 and 3) (Buzsáki et al., 2012; Kajikawa & Schroeder, 2011), consistent with complex evoked LFP responses in distal ipsilateral and contralateral cortical sites in response to electrical and optogenetic stimulation in rodents (Cavelli et al., 2022).

Given that the LFP reflects volume conduction and not only local activity (Buzsáki et al., 2012; Kajikawa & Schroeder, 2011), we examined CSD and population spiking of both stimulated and non-stimulated cortical regions (Figure 3). Deep cortical stimulation elicits measurable responses in both CSD and population spiking, whereas we were unable to detect such activations in non-stimulated cortical areas

from superficial stimulation. Similarly, Cavelli, Mao et al. (2022) showed that evoked laminar LFP responses were either undetectable or smaller when electrical stimulation was applied to the most superficial layers of the rat cortex compared to deeper layers, reflected by smaller PCI^{ST} values. The Neuropixels probes were inserted approximately perpendicular to the cortical surface. Deviation from perpendicular will impact the CSD derivation by effectively increasing the "effective" cortical thickness. This should not significantly affect the location of sources and sinks identified by the analysis.

The effects of electrical microstimulation are thought to be predominantly mediated by activation of axons (Gustafsson & Jankowska, 1976; Hao et al., 2016; Histed et al., 2009; Nowak & Bullier, 1998; Tehovnik et al., 2006). Therefore, the stronger evoked responses to deep stimulation could be due to activation of layer 5 and 6 cortico-thalamic cells via direct activation of axons that primarily terminate in thalamic regions (Figure 5), consistent with the literature suggesting that subcortical projecting, myelinated axons are more excitable than non-myelinated horizontal fibers within the cortex (Tehovnik & Slocum, 2013). Because most of the modulation in non-stimulated cortical regions occurs in the late time windows (25-300 ms after stimulation onset; Figure 4F), and the CSD analysis shows consistent sources/sinks across subjects only for late times (Figure 6A), we speculate that involvement of non-stimulated cortical areas is due to bursting in common thalamic projections and underscores the role of the CTC loop in perturbational complexity.

Limitations and benefits of studying ERPs in mice

There are qualitative differences between the ERPs we observed in mice and those in people (Casali et al., 2013; Comolatti et al., 2019; Ferrarelli et al., 2010; Massimini et al., 2005): most importantly, the two robust components (at 25 and 180 ms post-stimulation) in the ERPs from mice in quiet wakefulness are not apparent in human TMS-evoked EEG. Of course, there are several key differences between the brains of these two species, the most important being the three orders of magnitude difference in

volume and number of neurons. The mouse brain is roughly 0.5 cm^3 and contains 71 million neurons whereas the human brain is closer to 1200 cm^3 with 86 billion neurons (Herculano-Houzel et al., 2006; von Bartheld et al., 2016; Walløe et al., 2014). The smooth mouse neocortex is 0.8-1 mm thick, with 14 million neurons whereas the highly folded human neocortex is 2.5-3.0 mm thick with 16 billion neurons (Herculano-Houzel et al., 2006; Walløe et al., 2014). Recently, Bakken et al. (2021) published a comprehensive comparative analysis of cell types across human, marmoset, and mouse cortex. A key difference they highlight is more layer 2/3 intratelencephalic neurons in primates compared to mice, whereas layer 5 extratelencephalic and layer 6 corticothalamic neurons were significantly more common in mice. This is consistent with our findings that show pronounced cortico-thalamic activation and little evidence of wide-spread cortico-cortical activation in mice.

Another possible explanation for the striking difference in the ERPs between the two species is the different biophysical modes of stimulation – direct current flow from and to the inserted electrode versus a magnetic-field induced current flow in the cortical tissue underneath the TMS coil resting against the scalp. Electrical stimulation directly activates axons that run near the stimulation site, which can lead to antidromic activation of cell bodies and/or orthodromic propagation to the axon targets (Borchers et al., 2011; Gustafsson & Jankowska, 1976; Histed et al., 2009; Nowak & Bullier, 1998; Sombeck et al., 2022; Tehovnik et al., 2006; Tehovnik & Slocum, 2013; Terao & Ugawa, 2002), whereas TMS elicits indirect waves of cortical activation by exciting axons and neurons mainly trans-synaptically (Pashut et al., 2014; Siebner et al., 2022; Terao & Ugawa, 2002). However, there are also many similarities - stimulation in awake humans evokes a suppression of high frequencies, presumed to be an *off* period, close to the stimulated site (Pigorini et al., 2015). This is in line with the down-state we observe in mice, which highlights the role of the perturbational technique used for complexity measurements.

Despite these differences, this study led to novel and unexpected results linking the ERP to activity in the CTC loop. There are many additional open questions regarding neural mechanisms underlying spontaneous and stimulus-evoked EEG signals (Cohen, 2017). Rodent models offer a unique opportunity to combine EEG recordings with high-density extracellular recording technology to shine light on the underlying microcircuit dynamics. This study opens the door for future work with rodents using different perturbational techniques (e.g., chemogenetics, optogenetics [Cavelli et al., 2022], TMS [Senda et al., 2021]) to causally link the contributions of different cell types, brain regions, and network dynamics to EEG signals and ERP features commonly used in clinical and research settings.

ACKNOWLEDGEMENTS

We thank Anton Arkhipov, Matias Cavelli, Chiara Cirelli, Graham Findlay, Saurabh Gandhi, Soo Yeun Lee, Rong Mao, Marcello Massimini, Dana Mastrovito, Ethan McBride, David McCormick, Stefan Mihalas, Andrea Pigorini, Simone Sarasso, and Giulio Tononi for helpful discussions and intellectual contributions.

We thank the Animal Care and Lab Animal Services teams for mouse husbandry and care and the Manufacturing and Process Engineering team for experimental hardware and software support. We gratefully acknowledge funding from the Tiny Blue Dot Foundation for this study. We thank the Allen Institute founder, Paul G. Allen, for his vision, encouragement, and support.

AUTHOR CONTRIBUTIONS

Conceptualization and Methodology, L.D.C., I.R., S.R.O., and C.K.; Formal Analysis, L.D.C., I.R., and S.R.; Investigation, L.D.C., I.R., J.R.K., and L.C.M.; Data Curation, L.D.C., I.R., J.R.K., S.R., and L.C.M.; Writing – Original Draft, L.D.C., I.R., and C.K.; Writing – Review & Editing, L.D.C., I.R., J.R.K., S.R., L.C.M., S.R.O., and C.K.; Visualization, L.D.C.; Supervision, S.R.O. and C.K.; Funding Acquisition, C.K.

DECLARATION OF INTERESTS

C.K. is a Board Member and has a financial interest in *Intrinsic Powers Inc*. All other authors declare no competing interests.

METHODS

Experimental procedures closely followed those described in Siegle, Jia et al. (2021). A summary of these methods and details of procedures that differ are provided below.

Mice

Mice were maintained in the Allen Institute animal facility and used in accordance with protocols approved by the Allen Institute's Institutional Animal Care and Use Committee under protocols 1703 and 2003. All experiments used C57BL/6J wild-type mice (N=37). Male and female wild-type C57BL/6J mice were purchased from Jackson Laboratories (JAX stock #000664) at postnatal day 28 and they were 9-28 weeks old at the time of all *in vivo* electrophysiological recordings.

After surgery, all mice were single-housed and maintained on a reverse 12-h light cycle in a shared facility with room temperatures between 20 and 22 °C and humidity between 30 and 70%. All experiments were performed during the dark cycle. Mice had ad libitum access to food and water.

Surgical procedures and habituation

Each mouse went through the following order of procedures prior to the day of the experiment: 1) an initial sterile surgery to implant an EEG array and a titanium headframe for head-fixed electrophysiological experiments *in vivo*; 2) five days of recovery time post-surgery; 3) at least three weeks of habituation to head-fixation; 4) and a second sterile surgery to perform small craniotomies to allow for insertion of the stimulating electrode and Neuropixels probes.

One to three hours prior to each surgery, pre-operative injections of dexamethasone (3-4 mg/kg, IM) and ceftriaxone (100-125 mg/kg, SC) were administered. Mice were deeply anesthetized with isoflurane (5% isoflurane induction, 1.5-2.5% maintenance) and placed in a stereotaxic frame. Vital signs were monitored, body temperature was maintained at 37.5 °C with a heating pad under the animal (TC-1000 temperature controller, CWE, Inc.), and ocular lubricant (I Drop, VetPLUS) was applied to maintain hydration of the eyes during anesthesia. Atropine (0.02-0.05 mg/kg, SC) and carprofen (5-10 mg/kg, SC) were administered at the start of the procedure. After the surgical procedure, mice received an injection of lactated Ringer's solution (up to 1 mL, SC) and recovered on a heating pad. Animals received two days of analgesics and antibiotics post-surgery.

The initial surgery was performed on healthy mice that ranged in age from 5-20 weeks. Mice were deeply anesthetized prior to removing skin and exposing the skull. After leveling the skull, a 30-electrode mouse EEG array (NeuroNexus Technologies, Inc., Ann Arbor, Michigan) was carefully positioned on top of the skull and fixed in place with Kwik-Cast (World Precision Instruments, Inc., Sarasota, Florida). Skull screws were implanted either over the right olfactory bulb or left and right cerebellum that functioned as reference and ground for the EEG signals. White C&B Metabond (Parkell, Inc., Edgewood, New York) was then used to secure a custom titanium headframe and the EEG array to the skull. After five days of recovery, mice spent at least three weeks being habituated to handling and head-fixation.

Following habituation and up to one day before the recording, mice underwent the second surgical procedure. Under a microscope, the skull was exposed by drilling through the outer layer of Metabond then removing the Kwik-Cast and a small portion of the EEG polymer substrate, carefully avoiding damage to the EEG contacts. Up to three small craniotomies (less than 0.5 mm in diameter) were drilled to allow access to the brain regions of interest for the subsequent experiment. A small piece of artificial cerebrospinal fluid (**ACSF**)-soaked gel-foam sponge was positioned on top of each craniotomy and Kwik-

Cast was used to seal it. A 3D-printed plastic well was also fixed to the existing Metabond around the craniotomies.

In-vivo recording and stimulation

The day of the experiment, the mouse was placed on the running wheel and fixed to the headframe clamp with two set screws. Next, the thin layer of Kwik-Cast was removed to expose the craniotomies and abundant ACSF was added on top of the skull to prevent the exposed brain tissue from drying out. A 3D-printed cone was lowered to prevent the mouse's tail from contacting the probes and a black curtain was lowered over the front of the rig, placing the mouse in complete darkness.

EEG recording

All 30 EEG electrodes were connected to a 32-channel head-stage (RHD 32ch, Intan Technologies, Los Angeles, California) controlled by an Open Ephys acquisition board (Siegle et al., 2017). EEG signals were sampled at 2.5 kHz with a low-frequency cutoff of 0.1 Hz and digitized with 16-bit resolution. Each circular, platinum electrode on the EEG array had a diameter of 500 µm and an impedance of 0.01 MΩ (impedance measured by the manufacturer). All subjects had a skull screw implanted over the right cerebellum (penetrating the skull but not the dura) that served as electrical ground. One of the following served as a common refence electrode for the EEG signals: a 0.7 x 0.7 mm square platinum surface electrode above the left cerebellum, a skull screw implanted over the right olfactory bulb, or a skull screw implanted over the left cerebellum.

Neuropixels recording

In a subset of mice (N=26/37), simultaneous recordings from the EEG array and multiple Neuropixels probes (Jun et al., 2017) were performed. These experiments used Neuropixels 3a prototypes or standard Neuropixels 1.0 probes configured to record from the 384 electrodes closest to the tip of the probe. The signals from each recording site were split in hardware into a spike band (30 kHz sampling

rate, 500 Hz high-pass filter, 500x gain) and an LFP band (2.5 kHz sampling rate, 1,000 Hz low-pass filter, 250x gain) and data was acquired using the Open Ephys GUI (Siegle et al., 2017). Each probe was either connected to a dedicated FPGA streaming data over Ethernet (Neuropixels 3a) or a PXIe card inside a National Instruments chassis (Neuropixels 1.0).

The reference connection on the Neuropixels probes was permanently soldered to ground using a silver wire, and all recordings were made using either an external reference configuration (Neuropixels 3a) or a tip reference configuration (Neuropixels 1.0). All Neuropixels head-stage grounds, which were contiguous with the probe grounds, were connected in parallel to animal ground – a 32 AWG silver wire (A-M Systems, Sequim, Washington) placed in the ACSF on top of the craniotomies.

Neuropixels insertion

During the acute electrophysiological experiment, up to three Neuropixels probes were inserted targeting motor (MO), anterior cingulate (ACA), somatosensory (SS), visual (VIS), and thalamic nuclei. We restricted our analysis of thalamic nuclei to those that had strong projections to and/or from motor and somatosensory areas (Guo et al., 2017; J. A. Harris et al., 2019): anteroventral (AV), central lateral (CL), mediodorsal (MD), posterior (PO), reticular (RT), ventral anterior-lateral (VAL), ventral posterolateral (VPL), ventral posteromedial (VPM), and ventral medial (VM). We refer to these collectively as the somatomotor-related thalamic nuclei (SM-TH), disregarding the distinction between first and higher order thalamic regions.

The probe insertion process followed the steps detailed by Siegle, Jia et al. (2021). Briefly, each probe was individually inserted into the brain using a 3-axis micromanipulator (New Scale Technologies, Victor, New York) at a rate of 200 µm per min to a depth of 3.5 mm or less in the brain. After the probes reached their targets, they were allowed to settle for 10-15 min before starting the experiment. Before insertion, all Neuropixels probes were coated with a fluorescent dye (Vybrant DiI/DiO/DiD,

ThermoFisher Scientific, Waltham, Massachusetts) by repeatedly immersing them in a well filled with the dye and removing each probe slowly allowing the dye to dry on the surface.

Behavioral data and synchronization

The angular position of the running wheel and the synchronization signal for the electrical stimulus were acquired by a dedicated computer with a National Instruments card acquiring digital inputs at 100 kHz, which was considered the master clock. A 32-bit digital "barcode" was sent with an Arduino Uno (DEV-11021, SparkFun Electronics, Niwot, Colorado) every 30 s to synchronize all devices with the neural data from the EEG array and the Neuropixels probes. Details regarding the post-hoc data synchronization using the barcodes are described by Siegle, Jia et al. (2021).

Cortical Stimulation

Electrical stimulation was delivered through a custom bipolar platinum-iridium stereotrode (Microprobes for Life Science, Gaithersburg, Maryland) consisting of two parallel monopolar electrodes (50 kOhm impedance) with a vertical offset of 300 µm between the two tips. During each stage of the experiment, up to 120 biphasic, charge-balanced, cathodic-first current pulses (200 µs per phase, 3.5-4.5 s inter-stimulus interval) were delivered at three different current intensities (360 pulses total). The current intensities were chosen for each animal while it was awake before starting the experiment based on the following criteria: 1) the electrical pulse did not evoke any visible twitches and 2) the medium current elicited visible averaged evoked responses for most of the EEG electrodes ($n > 15$) defined as 3 standard deviations above baseline for at least 100 ms following the stimulus onset.

The stimulation electrode was acutely inserted using a 3-axis micromanipulator, like the Neuropixels probes. We targeted four locations for stimulation: secondary motor cortex (MOs), layer 2/3 (N=10 mice, 0.37±0.04 mm below the brain surface); MOs, layer 5/6 (N=11 mice, 1.15±0.06 mm below the brain surface); primary somatosensory cortex (SSp), layer 2/3 (N=8 mice, 0.47±0.06 mm below the brain

surface); and SSp, layer 5/6 (N=11 mice, 0.92±0.05 mm below the brain surface). Some mice received stimulation in multiple locations (N=10). Before insertion, the stimulation electrode was coated with a fluorescent dye, like the Neuropixels probes.

Experimental timeline

The paired EEG/Neuropixels recordings were acute, lasting 2-3 hours. At the beginning, awake head-fixed mice (free to run on or rest on the running wheel) were exposed to electrical stimuli after 5 min of baseline recording without stimulation. After the awake session, mice were anesthetized via inhaled isoflurane (5% induction) delivered through a small tube placed in front of the mouse's nose. Once a surgical level of anesthesia was reached, the animal was maintained unconscious by keeping the isoflurane level at 1-1.5%. The unconscious state was verified by lack of reaction to noxious stimuli such as toe or tail pinch and alcohol pad close to the nose of the animal. The EEG signals were also continuously monitored to avoid the burst suppression mode indicative of very deep anesthesia (Purdon et al., 2015). Then the same electrical stimuli session was repeated. While under anesthesia, we recorded the precise concentration of isoflurane delivered over time, in addition to the data streams listed above. Finally, the isoflurane was turned off and the mouse recovered. In a subset of mice (N=16), the electrical stimuli were delivered for a third (and sometimes a fourth) time during the recovery period. The resulting dataset allowed a direct comparison of the evoked neural responses across different brain states (quiet wakefulness, running, anesthetized, recovery).

Probe removal and cleaning

Upon completion of the experiment, probes were retracted from the brain at a rate of 1 mm/s. The craniotomies were protected with a small piece of ACSF-soaked gel-foam sponge and a thin layer of Kwik-Cast before mice were removed from head fixation and returned to their home cages overnight. The probes and the stimulating electrode were immersed in a well of 1% Tergazyme for around 2-6 h to remove residual tissue, and then rinsed in purified water.

Quality control for the EEG experiments

Overall EEG signal quality

Before the experiment, the EEG signals were tested by exposing the animal to visual flashes and evaluating the signal-to-noise ratio of the EEG evoked responses. Animals with low signal-to-noise ratio, high levels of 60 Hz noise, or large movement artifacts were not used for the experiment (8 mice).

EEG stimulation artifact

If more than half of the EEG channels over the course of the experiment showed large stimulation artifacts lasting for hundreds of milliseconds after the stimulation onset, the session was excluded (8 sessions across 6 mice). In total, out of 37 implanted mice, 23 were included in the study.

Ex vivo imaging and localization of electrodes

After the experiment, mice were deeply anesthetized (5% isoflurane) and perfused with 4% paraformaldehyde. The brains were preserved in 4% paraformaldehyde for 48 hours, rinsed with 1x PBS, and stored at 4 °C in PBS. The brains were then processed in one of two ways: brains were sliced into 100 µm coronal sections using a vibratome (Leica VT1000S) and imaged with a fluorescent microscope (Olympus VS110/120) at 10x magnification or whole brains were imaged using serial two-photon tomography (Oh et al., 2014; Ragan et al., 2012).

Images of the 100 µm coronal sections were aligned to the Allen Institute Common Coordinate Framework (CCFv3) following the process detailed by McBride et al. (2022) and images from serial two-photon tomography were aligned to the CCFv3 following the process detailed by Oh et al. (2014). Fluorescent tracks corresponding to the location of the Neuropixels probes and the stimulation electrode were manually identified in the aligned images. Because each CCFv3 coordinate corresponds to a unique brain region, the precision of brain region assignments is determined by the resolution of the CCFv3, which was 25 µm per pixel. For each Neuropixels probe the locations of major structural

boundaries along the track was manually aligned with the physiology data (Liu et al., 2021; Siegle et al., 2021). Then each recording channel along the Neuropixels probe (and associated neurons) was assigned to a unique CCFv3 structure. Other studies have reported better than 0.1 mm accuracy for electrode localization following similar methods (Liu et al., 2021).

Data processing

Stimulus artifact masking

In all recordings we observed short latency voltage transients time-locked to the stimulus. Though the stimulus had a total duration of 0.4 ms, artifacts sometimes lasted up to 2 ms. To mask the artifact, the raw signal from -2 to 0 ms was copied, reversed, and replaced the 0 to 2 ms artifact window. The same masking procedure was used across all electrophysiology data types.

EEG

After artifact masking, EEG recordings were visually inspected to identify electrodes containing noise artifacts or remaining large and long stimulation artifacts. These were excluded from further analysis, leaving an average of 23 +/- 4 artifact-free electrodes out of 30 for each subject. EEG signals from all good electrodes were re-referenced to the common average across electrodes and bandpass filtered from 0.1 to 100 Hz (Butterworth filter, 3rd order). Finally, the continuous EEG signals were segmented into epochs from -2 to +2 s from stimulus onset and saved for further analysis.

Neuropixels LFP

After artifact masking, LFP signals were down sampled from 2.5 kHz to 1.25 kHz after applying an anti-aliasing filter. The signals were then high pass filtered (Butterworth filter, 1st order) and re-referenced to the median signal from electrodes that were in the ACSF above the brain surface (to remove common signal from the tip reference electrode). Finally, the continuous LFP signals were segmented into epochs from -2 to +2 s from stimulus onset and saved for further analysis.

Neuropixels CSD

The preprocessed LFP epochs underwent an automatic channel rejection based on Chebyshev's inequality, iteratively interpolating any channel whose amplitude instantaneously exceeded ±7 standard deviations with respect to the others (Russo et al., 2021). The cleaned LFP voltages where smoothed in the time (window=8 ms) and space domain (1st smoothing window=26 channels; 2nd smoothing window=4 channels). The CSD was calculated as the second spatial derivative (Mitzdorf, 1985) from the cleaned, smoothed LFP signals. The CSD formulation employed assumes an ohmic conductive medium, constant extracellular conductivity (σ=0.3 S/m), and homogeneous in-plane neuronal activity, with the boundary condition of zero current outside the sampled area.

Spike sorting

After applying the artifact masking to the raw spike band data, it was pre-processed and spike-sorted using Kilosort 2.0 (Stringer et al., 2019) as described by Siegle, Jia et al. (2021). After spike sorting, any spikes that occurred during the artifact window (0 to +2 ms from stimulus onset) were removed from further analysis. High quality units were identified for further analysis using metrics described by Siegle, Jia et al. (2021). We classified regular spiking (**RS**) and fast spiking (**FS**) neurons (putative pyramidal and inhibitory neurons, respectively) based on their spike waveform duration (RS duration > 4 ms; FS duration ≤ 0.4 ms) (Barthó et al., 2004; Bortone et al., 2014; Bruno & Simons, 2002; Jia et al., 2016; Niell & Stryker, 2008; Sirota et al., 2008).

Data Analysis

EEG event-related potentials (ERPs)

Across each experiment, trials were classified by the behavioral state of the animal: quiet wakefulness, if the mouse's speed (measured by the wheel's angular velocity) was equal to 0 cm/s from -0.5 to +0.5 s from the stimulus onset; running, if the mouse's speed was greater than 0 cm/s; anesthetized, when the

mouse was unconscious; and recovery, after the isoflurane delivery was discontinued. ERPs associated with a given state were then compiled by averaging all EEG traces assigned to that state.

ERP magnitude and duration

To quantify the ERP metrics, the trial-averaged EEG signals (-2 to +2 s after stimulus onset) were used to calculate the global field power (global mean field power) by taking the standard deviation across all channels for every time point (Cohen, 2014; Esser et al., 2006; Lehmann & Skrandies, 1980). Next, the z-score of the global field power was computed relative to baseline values (-2 to 0 s). The duration of the response was measured as the length of time the global field power (z-score) was greater than three standard deviations above baseline (z=3) in the response window (0 to +2 s). The magnitude of the response was calculated by integrating under the global field power (z-score) but above z=3 in the response window and dividing it by the area under the baseline window (see Figure 1-figure supplement 2).

LFP, CSD, and population spiking magnitude

To quantify the magnitude of the evoked LFP and CSD response, the spatial average of the rectified, trial averaged signals for all channels in the respective cortical region, all layers except for layer 1. Then the area under the curve was calculated for the post-stimulus period (0 to +0.5 s) of the grand average (z-score of the baseline). A similar procedure was used for the population spiking, except the signals used were single neuron spike density functions. For all data types, the magnitude of the background activity was determined using a permutation test to shuffle the event onset time per trial (n=1000 shuffles), thus creating a distribution of null values representing the area under the curve of the background activity. The response magnitude was then calculated by subtracting the mean of the onset-shuffled values and dividing by the standard deviation.

Significantly modulated neurons

The fraction of neurons modulated by the electrical stimulation was quantified following the method detailed by McBride et al. (2022). Briefly, for each neuron pre- and post-stimulus spikes were counted on a trial-by-trial basis for the specified windows: 2-25 ms, 25-150 ms, and 150-300 ms. The duration of the window was always matched for pre- and post-stimulus. Then a Wilcoxon signed-rank test was performed on the trial-wise pre- and post-stimulus spike counts to obtain a p-value. The p-values obtained for all RS neurons in all areas of interest were corrected using the Benjamini-Hochberg correction with the false discovery rate set at 0.05. Neurons with an adjusted p-value < 0.05 were considered significantly modulated. They were labeled as "increased" or "decreased" based on whether their spike count increased or decreased, respectively, in the post-stimulus window relative to the pre-stimulus window on average.

Population CSD

To compare CSD across mice, we transformed each CSD trace to a homogeneous space (10 bins per layer) through a non-linear transform. Significantly consistent activations were assessed through a Wilcoxon signed-rank test (threshold $p<0.05$). Isolated significant bins (i.e., not surrounded by significant bins in both space and time) were removed.

Perturbational Complexity Index, state-transition (PCI^{ST})

PCI^{ST} was used to evaluate the spatiotemporal complexity of the EEG ERPs for each brain state (Comolatti et al., 2019). PCI^{ST} was computed using the code available at github.com/renzocom/PCIst and the parameters were set as follows: baseline window = [-0.8, -0.002] s; response window = [0.002, 0.8] s; minimum SNR = 1.6; maximum variance = 99%; and the parameter k = 1.2. In all calculations, the number of trials per state within subject was matched.

Statistics

Statistical analysis was performed in Python. All data was tested for normality using the Shapiro-Wilk test from the SciPy package (scipy.stats.shapiro). For normally distributed datasets we used the unpaired t-test (scipy.stats.ttest_ind) or the paired t-test (scipy.stats.ttest_rel). For non-parametric datasets we used the Mann-Whitney U test (scipy.stats.mannwhitneyu) or the Wilcoxon signed-rank test (scipy.stats.wilcoxon). All comparisons using t-tests are two-sided. Statistical comparisons between multiple groups were performed using both parametric (ANOVA) and non-parametric (Friedman) tests with post hoc, pairwise comparisons corrected for multiple comparisons using Benjamini-Hochberg false discovery rate. Correlational analyses were performed using Pearson correlation coefficients.

In all figures, the convention is * weak evidence to reject null hypothesis ($0.05 > p > 0.01$), ** strong evidence to reject null hypothesis ($0.01 > p > 0.001$), *** very strong evidence to reject null hypothesis ($0.001 > p$). The values in the text indicate the mean and standard error of the mean (mean ± SEM) or the median and IQR [25th and 75th percentiles] for normally distributed and non-parametric datasets, respectively.

DATA AVAILABILITY

The data generated and analyzed in this manuscript are publicly available in Neurodata Without Borders (NWB) format (Rübel et al., 2022) in the DANDI Archive.

Claar, Leslie D; Rembado, Irene; Kuyat, Jacqulyn R; Russo, Simone; Marks, Lydia C; Olsen, Shawn R; Koch, Christof (2023) Simultaneous electroencephalography, extracellular electrophysiology, and cortical electrical stimulation in head-fixed mice (Version 0.230317.0039) [Data set]. DANDI archive. https://dandiarchive.org/dandiset/000458/0.230317.0039

REFERENCES

Arena, A., Comolatti, R., Thon, S., Casali, A. G., & Storm, J. F. (2021). General Anesthesia Disrupts Complex Cortical Dynamics in Response to Intracranial Electrical Stimulation in Rats. *ENeuro*, *8*(4). https://doi.org/10.1523/ENEURO.0343-20.2021

Aru, J., Suzuki, M., & Larkum, M. E. (2020). Cellular Mechanisms of Conscious Processing. *Trends in Cognitive Sciences*, *24*(10), 814–825. https://doi.org/10.1016/j.tics.2020.07.006

Bai, Y., Lin, Y., & Ziemann, U. (2021). Managing disorders of consciousness: the role of electroencephalography. In *Journal of Neurology* (Issue 268). Springer Berlin Heidelberg. https://doi.org/10.1007/s00415-020-10095-z

Bai, Y., Xia, X., & Li, X. (2017). A review of resting-state electroencephalography analysis in disorders of consciousness. *Frontiers in Neurology*, *8*(SEP), 471. https://doi.org/10.3389/FNEUR.2017.00471

Bakken, T. E., Jorstad, N. L., Hu, Q., Lake, B. B., Tian, W., Kalmbach, B. E., Crow, M., Hodge, R. D., Krienen, F. M., Sorensen, S. A., Eggermont, J., Yao, Z., Aevermann, B. D., Aldridge, A. I., Bartlett, A., Bertagnolli, D., Casper, T., Castanon, R. G., Crichton, K., … Lein, E. S. (2021). Comparative cellular analysis of motor cortex in human, marmoset and mouse. *Nature*, *598*(7879), 111–119. https://doi.org/10.1038/s41586-021-03465-8

Bal, T., Debay, D., & Destexhe, A. (2000). Cortical Feedback Controls the Frequency and Synchrony of Oscillations in the Visual Thalamus. *Journal of Neuroscience*, *20*(19), 7478–7488. https://doi.org/10.1523/JNEUROSCI.20-19-07478.2000

Barthó, P., Hirase, H., Monconduit, L., Zugaro, M., Harris, K. D., & Buzsáki, G. (2004). Characterization of Neocortical Principal Cells and Interneurons by Network Interactions and Extracellular Features. *Journal of Neurophysiology*, *92*(1), 600–608. https://doi.org/10.1152/jn.01170.2003

Bharioke, A., Munz, M., Brignall, A., Kosche, G., Eizinger, M. F., Ledergerber, N., Hillier, D., Gross-Scherf, B., Conzelmann, K.-K., Macé, E., & Roska, B. (2022). General anesthesia globally synchronizes activity selectively in layer 5 cortical pyramidal neurons. *Neuron*, *110*(12), 2024-2040.e10. https://doi.org/10.1016/J.NEURON.2022.03.032

Borchers, S., Himmelbach, M., Logothetis, N., & Karnath, H. O. (2011). Direct electrical stimulation of human cortex — the gold standard for mapping brain functions? *Nature Reviews Neuroscience*, *13*(1), 63–70. https://doi.org/10.1038/nrn3140

Borden, P. Y., Wright, N. C., Morrissette, A. E., Jaeger, D., Haider, B., Correspondence, G. B. S., & Stanley, G. B. (2022). Thalamic bursting and the role of timing and synchrony in thalamocortical signaling in the awake mouse. *Neuron*, *110*, 2836–2853. https://doi.org/10.1016/j.neuron.2022.06.008

Bortone, D. S., Olsen, S. R., & Scanziani, M. (2014). Translaminar Inhibitory Cells Recruited by Layer 6 Corticothalamic Neurons Suppress Visual Cortex. *Neuron*, *82*, 474–485. https://doi.org/10.1016/j.neuron.2014.02.021

Bruno, R. M., & Simons, D. J. (2002). Feedforward Mechanisms of Excitatory and Inhibitory Cortical Receptive Fields. *The Journal of Neuroscience*, *22*(24), 10966–10975. https://doi.org/10.1523/JNEUROSCI.22-24-10966.2002

Butovas, S., Hormuzdi, S. G., Monyer, H., & Schwarz, C. (2006). Effects of electrically coupled inhibitory networks on local neuronal responses to intracortical microstimulation. *Journal of*

Neurophysiology, *96*(3), 1227–1236. https://doi.org/10.1152/jn.01170.2005

Butovas, S., & Schwarz, C. (2003). Spatiotemporal Effects of Microstimulation in Rat Neocortex: A Parametric Study Using Multielectrode Recordings. *Journal of Neurophysiology*, *90*, 3024–3039. https://doi.org/10.1152/jn.00245.2003

Buzsáki, G., Anastassiou, C. A., & Koch, C. (2012). The origin of extracellular fields and currents — EEG, ECoG, LFP and spikes. *Nature Reviews Neuroscience*, *13*(6), 407–420. https://doi.org/10.1038/nrn3241

Casali, A. G., Gosseries, O., Rosanova, M., Boly, M., Sarasso, S., Casali, K. R., Casarotto, S., Bruno, M. A., Laureys, S., Tononi, G., & Massimini, M. (2013). A theoretically based index of consciousness independent of sensory processing and behavior. *Science Translational Medicine*, *5*(198). https://doi.org/10.1126/scitranslmed.3006294

Casarotto, S., Comanducci, A., Rosanova, M., Sarasso, S., Fecchio, M., Napolitani, M., Pigorini, A., Casali, A. G., Trimarchi, P. D., Boly, M., Gosseries, O., Bodart, O., Curto, F., Landi, C., Mariotti, M., Devalle, G., Laureys, S., Tononi, G., & Massimini, M. (2016). Stratification of Unresponsive Patients by an Independently Validated Index of Brain Complexity. *Annals of Neurology*, *80*(5), 718–729. https://doi.org/10.1002/ana.24779

Cavelli, M. L., Mao, R., Findlay, G., Driessen, K., Bugnon, T., Tononi, G., & Cirelli, C. (2022). Sleep/wake changes in perturbational complexity in rats and mice. *BioRxiv*, 2022.08.02.502525. https://doi.org/10.1101/2022.08.02.502525

Chung, S., & Ferster, D. (1998). Strength and orientation tuning of the thalamic input to simple cells revealed by electrically evoked cortical suppression. *Neuron*, *20*(6), 1177–1189. https://doi.org/10.1016/S0896-6273(00)80498-5

Claudi, F., Tyson, A. L., Petrucco, L., Margrie, T. W., Portugues, R., & Branco, T. (2021). Visualizing anatomically registered data with brainrender. *ELife*, *10*. https://doi.org/10.7554/ELIFE.65751

Cohen, M. X. (2014). Analyzing Neural Time Series Data: Theory and Practice. In *Analyzing Neural Time Series Data*. The MIT Press. https://doi.org/10.7551/MITPRESS/9609.001.0001

Cohen, M. X. (2017). Where Does EEG Come From and What Does It Mean? *Trends in Neurosciences*, *40*(4), 208–218. https://doi.org/10.1016/j.tins.2017.02.004

Comolatti, R., Pigorini, A., Casarotto, S., Fecchio, M., Faria, G., Sarasso, S., Rosanova, M., Gosseries, O., Boly, M., Bodart, O., Ledoux, D., Brichant, J.-F., Nobili, L., Laureys, S., Tononi, G., Massimini, M., & Casali, A. G. (2019). A fast and general method to empirically estimate the complexity of brain responses to transcranial and intracranial stimulations. *Brain Stimulation*. https://doi.org/10.1016/J.BRS.2019.05.013

Contreras, D., & Steriade, M. (1995). Cellular Basis of EEG Slow Rhythms: A Study of Dynamic Corticothalamic Relationships. *The Journal of Neuroscience*, *15*(1), 604–622. https://doi.org/10.1523/JNEUROSCI.15-01-00604.1995

D'Andola, M., Rebollo, B., Casali, A. G., Weinert, J. F., Pigorini, A., Villa, R., Massimini, M., & Sanchez-Vives, M. V. (2018). Bistability, Causality, and Complexity in Cortical Networks: An In Vitro Perturbational Study. *Cerebral Cortex*, *28*(7), 2233–2242. https://doi.org/10.1093/cercor/bhx122

Dasilva, M., Camassa, A., Navarro-Guzman, A., Pazienti, A., Perez-Mendez, L., Zamora-López, G., Mattia,

M., & Sanchez-Vives, M. V. (2021). Modulation of cortical slow oscillations and complexity across anesthesia levels. *NeuroImage*, *224*, 117415. https://doi.org/10.1016/j.neuroimage.2020.117415

Domich, L., Oakson, G., & Steriade, M. (1986). Thalamic burst patterns in the naturally sleeping cat: a comparison between cortically projecting and reticularis neurones. *The Journal of Physiology*, *379*(1), 429–449. https://doi.org/10.1113/JPHYSIOL.1986.SP016262

Douglas, R. J., & Martin, K. A. C. (1991). A Functional Microcircuit for Cat Visual Cortex. *Journal of Physiology*, *440*, 735–769. https://doi.org/10.1113/jphysiol.1991.sp018733

Esser, S. K., Huber, R., Massimini, M., Peterson, M. J., Ferrarelli, F., & Tononi, G. (2006). A direct demonstration of cortical LTP in humans: A combined TMS/EEG study. *Brain Research Bulletin*, *69*(1), 86–94. https://doi.org/10.1016/J.BRAINRESBULL.2005.11.003

Farisco, M., Pennartz, C., Annen, J., Cecconi, B., & Evers, K. (2022). Indicators and criteria of consciousness: ethical implications for the care of behaviorally unresponsive patients. *BMC Medical Ethics*, *23*. https://doi.org/10.1186/s12910-022-00770-3

Ferrarelli, F., Massimini, M., Sarasso, S., Casali, A., Riedner, B. A., Angelini, G., Tononi, G., & Pearce, R. A. (2010). Breakdown in cortical effective connectivity during midazolam-induced loss of consciousness. *Proceedings of the National Academy of Sciences of the United States of America*, *107*(6), 2681–2686. https://doi.org/10.1073/pnas.0913008107

Franken, P., Malafosse, A., & Tafti, M. (1999). Genetics of sleep regulation in mice-Franken et al Genetic Determinants of Sleep Regulation in Inbred Mice. *SLEEP*, *22*(2). https://academic.oup.com/sleep/article/22/2/155/2731698

Freeman, J. A., & Nicholson, C. (1975). Experimental optimization of current source-density technique for anuran cerebellum. *Journal of Neurophysiology*, *38*(2), 369–382. https://doi.org/10.1152/JN.1975.38.2.369

Frohlich, J., Toker, D., & Monti, M. M. (2021). Consciousness among delta waves: A paradox? *Brain*, *144*(8), 2257–2277. https://doi.org/10.1093/brain/awab095

Grenier, F., Timofeev, I., & Steriade, M. (1998). Leading role of thalamic over cortical neurons during postinhibitory rebound excitation. *Proceedings of the National Academy of Sciences of the United States of America*, *95*(23), 13929–13934. https://doi.org/10.1073/pnas.95.23.13929

Guido, W., & Weyand, T. (1995). Burst responses in thalamic relay cells of the awake behaving cat. *Journal of Neurophysiology*, *74*(4), 1782–1786. https://doi.org/10.1152/JN.1995.74.4.1782

Guo, Z. V., Inagaki, H. K., Daie, K., Druckmann, S., Gerfen, C. R., & Svoboda, K. (2017). Maintenance of persistent activity in a frontal thalamocortical loop. *Nature*, *545*(7653), 181–186. https://doi.org/10.1038/nature22324

Gustafsson, B., & Jankowska, E. (1976). Direct and Indirect Activation of Nerve Cells by Electrical Pulses Applied Extracellularly. *Journal of Physiology*, *258*, 33–61. https://doi.org/10.1113/jphysiol.1976.sp011405

Halassa, M. M., Siegle, J. H., Ritt, J. T., Ting, J. T., Feng, G., & Moore, C. I. (2011). Selective optical drive of thalamic reticular nucleus generates thalamic bursts and cortical spindles. *Nature Neuroscience*, *14*(9), 1118–1120. https://doi.org/10.1038/nn.2880

Hao, Y., Riehle, A., & Brochier, T. G. (2016). Mapping horizontal spread of activity in monkey motor cortex using single pulse microstimulation. *Frontiers in Neural Circuits*, *10*(DEC), 104. https://doi.org/10.3389/FNCIR.2016.00104

Harris, J. A., Mihalas, S., Hirokawa, K. E., Whitesell, J. D., Choi, H., Bernard, A., Bohn, P., Caldejon, S., Casal, L., Cho, A., Feiner, A., Feng, D., Gaudreault, N., Gerfen, C. R., Graddis, N., Groblewski, P. A., Henry, A. M., Ho, A., Howard, R., … Zeng, H. (2019). Hierarchical organization of cortical and thalamic connectivity. *Nature*, *575*. https://doi.org/10.1038/s41586-019-1716-z

Harris, K. D., & Shepherd, G. M. G. (2015). The neocortical circuit: Themes and variations. *Nature Neuroscience*, *18*(2), 170–181. https://doi.org/10.1038/nn.3917

Herculano-Houzel, S., Mota, B., & Lent, R. (2006). Cellular scaling rules for rodent brains. *Proceedings of the National Academy of Sciences of the United States of America*, *103*(32), 12138–12143. https://doi.org/10.1073/PNAS.0604911103

Hill, S., & Tononi, G. (2005). Modeling sleep and wakefulness in the thalamocortical system. *Journal of Neurophysiology*, *93*(3), 1671–1698. https://doi.org/10.1152/JN.00915.2004

Histed, M. H., Bonin, V., & Reid, R. C. (2009). Direct Activation of Sparse, Distributed Populations of Cortical Neurons by Electrical Microstimulation. *Neuron*, *63*(4), 508–522. https://doi.org/10.1016/j.neuron.2009.07.016

Hooks, B. M., Mao, T., Gutnisky, D. A., Yamawaki, N., Svoboda, K., & Shepherd, G. M. G. (2013). Organization of Cortical and Thalamic Input to Pyramidal Neurons in Mouse Motor Cortex. *The Journal of Neuroscience*, *33*(2), 748–760. https://doi.org/10.1523/JNEUROSCI.4338-12.2013

Jia, X., Siegle, J., Bennett, C., Gale, S., Denman, D. R., Koch, C., & Olsen, S. (2016). High-density extracellular probes reveal dendritic backpropagation and facilitate neuron classification 1 2. *Journal of Neurophysiology*, *121*(5), 1831–1847. https://doi.org/10.1101/376863

Jonak, C. R., Lovelace, J. W., Ethell, I. M., Razak, K. A., & Binder, D. K. (2018). Reusable Multielectrode Array Technique for Electroencephalography in Awake Freely Moving Mice. *Frontiers in Integrative Neuroscience*, *12*, 53. https://doi.org/10.3389/fnint.2018.00053

Jun, J. J., Steinmetz, N. A., Siegle, J. H., Denman, D. J., Bauza, M., Barbarits, B., Lee, A. K., Anastassiou, C. A., Andrei, A., Aydin, Ç., Barbic, M., Blanche, T. J., Bonin, V., Couto, J., Dutta, B., Gratiy, S. L., Gutnisky, D. A., Häusser, M., Karsh, B., … Harris, T. D. (2017). Fully integrated silicon probes for high-density recording of neural activity. *Nature*, *551*(7679), 232–236. https://doi.org/10.1038/nature24636

Kajikawa, Y., & Schroeder, C. E. (2011). How local is the local field potential? *Neuron*, *72*(5), 847–858. https://doi.org/10.1016/J.NEURON.2011.09.029

Kara, P., Pezaris, J. S., Yurgenson, S., & Reid, R. C. (2002). The spatial receptive field of thalamic inputs to single cortical simple cells revealed by the interaction of visual and electrical stimulation. *Proceedings of the National Academy of Sciences of the United States of America*, *99*(25), 16261–16266. https://doi.org/10.1073/pnas.242625499

Kobylarz, E. J., & Schiff, N. D. (2005). Neurophysiological correlates of persistent vegetative and minimally conscious states. *Neuropsychological Rehabilitation*, *15*, 323–332. https://doi.org/10.1080/09602010443000605

Koch, C., Massimini, M., Boly, M., & Tononi, G. (2016). Neural correlates of consciousness: progress and problems. *Nature Reviews Neuroscience*, *17*, 307–321. https://doi.org/10.1038/nrn.2016.22

Kondziella, D., Bender, A., Diserens, K., van Erp, W., Estraneo, A., Formisano, R., Laureys, S., Naccache, L., Ozturk, S., Rohaut, B., Sitt, J. D., Stender, J., Tiainen, M., Rossetti, A. O., Gosseries, O., & Chatelle, C. (2020). European Academy of Neurology guideline on the diagnosis of coma and other disorders of consciousness. *European Journal of Neurology*, *27*(5), 741–756. https://doi.org/10.1111/ENE.14151

Land, R., Kapche, A., Ebbers, L., & Kral, A. (2019). 32-channel mouse EEG: Visual evoked potentials. *Journal of Neuroscience Methods*, 108316. https://doi.org/10.1016/j.jneumeth.2019.108316

Larkum, M. (2013). A cellular mechanism for cortical associations: an organizing principle for the cerebral cortex. *Trends in Neurosciences*, *36*(3), 141–151. https://doi.org/10.1016/J.TINS.2012.11.006

Lehmann, D., & Skrandies, W. (1980). Reference-free identification of components of checkerboard-evoked multichannel potential fields. *Electroencephalography and Clinical Neurophysiology*, *48*(6), 609–621. https://doi.org/10.1016/0013-4694(80)90419-8

Liu, L. D., Chen, S., Hou, H., West, S. J., Faulkner, M., Laboratory, T. I. B., Economo, M. N., Li, N., & Svoboda, K. (2021). Accurate Localization of Linear Probe Electrode Arrays across Multiple Brains. *ENeuro*, *8*(6). https://doi.org/10.1523/ENEURO.0241-21.2021

Logothetis, N. K., Augath, M. A., Murayama, Y., Rauch, A., Sultan, F. F., Goense, J., Oeltermann, A., & Merkle, H. (2010). The Effects of Electrical Microstimulation on Cortical Signal Propagation. *Nature Neuroscience*, *13*(10), 1283–1293. https://doi.org/10.1038/nn.2631

Lu, S. M., Guido, W., & Sherman, S. M. (1992). Effects of membrane voltage on receptive field properties of lateral geniculate neurons in the cat: contributions of the low-threshold Ca2+ conductance. *Journal of Neurophysiology*, *68*(6), 2185–2198. https://doi.org/10.1152/JN.1992.68.6.2185

Massimini, M., Ferrarelli, F., Huber, R., Esser, S. K., Singh, H., & Tononi, G. (2005). Breakdown of Cortical Effective Connectivity During Sleep. *Science*, *309*(5744), 2228–2232. https://doi.org/10.1016/j.cogbrainres.2004.10.022

McBride, E. G., Gandhi, S. R., Kuyat, J. R., Ollerenshaw, D. R., Arkhipov, A., Koch, C., & Olsen, S. R. (2022). Influence of claustrum on cortex varies by area, layer, and cell type. *Neuron*. https://doi.org/10.1016/J.NEURON.2022.10.026

McGinley, M. J., David, S. V., & McCormick, D. A. (2015). Cortical Membrane Potential Signature of Optimal States for Sensory Signal Detection. *Neuron*, *87*(1), 179–192. https://doi.org/10.1016/j.neuron.2015.05.038

Mitzdorf, U. (1985). Current Source-Density Method and Application in Cat Cerebral Cortex: Investigation of Evoked Potentials and EEG Phenomena. *Physiological Reviews*, *65*(1), 37–100.

Nestvogel, D. B., & McCormick, D. A. (2021). Visual thalamocortical mechanisms of waking state-dependent activity and alpha oscillations. *Neuron*, *0*(0). https://doi.org/10.1016/J.NEURON.2021.10.005

Niell, C. M., & Stryker, M. P. (2008). Highly selective receptive fields in mouse visual cortex. *Journal of Neuroscience*, *28*(30), 7520–7536. https://doi.org/10.1523/JNEUROSCI.0623-08.2008

Nowak, L. G., & Bullier, J. (1998). Axons, but not cell bodies, are activated by electrical stimulation in cortical gray matter. II. Evidence from selective inactivation of cell bodies and axon initial segments. *Experimental Brain Research*, *118*(4), 489–500. https://doi.org/10.1007/S002210050305/METRICS

Oh, S. W., Harris, J. A., Ng, L., Winslow, B., Cain, N., Mihalas, S., Wang, Q., Lau, C., Kuan, L., Henry, A. M., Mortrud, M. T., Ouellette, B., Nguyen, T. N., Sorensen, S. A., Slaughterbeck, C. R., Wakeman, W., Li, Y., Feng, D., Ho, A., … Zeng, H. (2014). A mesoscale connectome of the mouse brain. *Nature*, *508*. https://doi.org/10.1038/nature13186

Pashut, T., Magidov, D., Ben-Porat, H., Wolfus, S., Friedman, A., Perel, E., Lavidor, M., Bar-Gad, I., Yeshurun, Y., & Korngreen, A. (2014). Patch-clamp recordings of rat neurons from acute brain slices of the somatosensory cortex during magnetic stimulation. *Frontiers in Cellular Neuroscience*, *8*(JUN), 1–12. https://doi.org/10.3389/fncel.2014.00145

Patrick L. Purdon, P. ., Aaron Sampson, B. S., Kara J. Pavone, B. S., & Emery N. Brown, M.D., P. D. (2015). Clinical Electroencephalography for Anesthesiologists- Part I- Background and Basic Signatures. *Anesthesiology*, *123*(4), 937–960. https://doi.org/10.1097/ALN.0000000000000841

Pigorini, A., Sarasso, S., Proserpio, P., Szymanski, C., Arnulfo, G., Casarotto, S., Fecchio, M., Rosanova, M., Mariotti, M., Lo Russo, G., Palva, J. M., Nobili, L., & Massimini, M. (2015). Bistability breaks-off deterministic responses to intracortical stimulation during non-REM sleep. *NeuroImage*, *112*, 105–113. https://doi.org/10.1016/J.NEUROIMAGE.2015.02.056

Pinault, D. (2004). The thalamic reticular nucleus: structure, function and concept. *Brain Research Reviews*, *46*(1), 1–31. https://doi.org/10.1016/J.BRAINRESREV.2004.04.008

Ragan, T., Kadiri, L. R., Umadevi Venkataraju, K., Bahlmann, K., Sutin, J., Taranda, J., Arganda-Carreras, I., Kim, Y., Seung, H. S., & Osten, P. (2012). Serial two-photon tomography: an automated method for ex-vivo mouse brain imaging HHS Public Access. *Nature Methods*, *9*(3), 255–258. https://doi.org/10.1038/nmeth.1854

Ramcharan, E. J., Gnadt, J. W., & Sherman, S. M. (2005). Higher-order thalamic relays burst more than first-order relays. *Proceedings of the National Academy of Sciences of the United States of America*, *102*(34), 12236–12241. https://doi.org/10.1073/PNAS.0502843102

Ries, C. R., & Puil, E. (1999). Mechanism of anesthesia revealed by shunting actions of isoflurane on thalamocortical neurons. *Journal of Neurophysiology*, *81*(4), 1795–1801. https://doi.org/10.1152/jn.1999.81.4.1795

Rosanova, M., Fecchio, M., Casarotto, S., Sarasso, S., Casali, A. G., Pigorini, A., Comanducci, A., Seregni, F., Devalle, G., Citerio, G., Bodart, O., Boly, M., Gosseries, O., Laureys, S., & Massimini, M. (2018). Sleep-like cortical OFF-periods disrupt causality and complexity in the brain of unresponsive wakefulness syndrome patients. *Nature Communications*, *9*, 1–10. https://doi.org/10.1038/s41467-018-06871-1

Roux, L., Stark, E., Sjulson, L., & Buzsáki, G. (2014). In vivo optogenetic identification and manipulation of GABAergic interneuron subtypes. *Current Opinion in Neurobiology*, *26*, 88–95. https://doi.org/10.1016/j.conb.2013.12.013

Rübel, O., Tritt, A., Ly, R., Dichter, B. K., Ghosh, S., Niu, L., Baker, P., Soltesz, I., Ng, L., Svoboda, K., Frank, L., & Bouchard, K. E. (2022). The Neurodata Without Borders ecosystem for neurophysiological

data science. *ELife*, *11*, e78362. https://doi.org/10.7554/ELIFE.78362

Russo, S., Pigorini, A., Mikulan, E., Sarasso, S., Rubino, A., Zauli, F. M., Parmigiani, S., d'Orio, P., Cattani, A., Francione, S., Tassi, L., Bassetti, C. L. A., Lo Russo, G., Nobili, L., Sartori, I., & Massimini, M. (2021). Focal lesions induce large-scale percolation of sleep-like intracerebral activity in awake humans. *NeuroImage*, *234*, 117964. https://doi.org/10.1016/J.NEUROIMAGE.2021.117964

Sachidhanandam, S., Sreenivasan, V., Kyriakatos, A., Kremer, Y., & Petersen, C. C. H. (2013). Membrane potential correlates of sensory perception in mouse barrel cortex. *Nature Neuroscience*, *16*(11), 1671–1677. https://doi.org/10.1038/nn.3532

Schiff, N. D., Nauvel, T., & Victor, J. D. (2014). Large-Scale Brain Dynamics in Disorders of Consciousness. *Current Opinion in Neurobiology*, *0*, 7. https://doi.org/10.1016/J.CONB.2013.10.007

Senda, D., Strong, H., Hines, D., Hines, R., & Baker, R. J. (2021). A compact 1200 V, 700 A, IGBT-based pulse generator for repetitive transcranial magnetic stimulation in vivo laboratory experiments on small animals. *Review of Scientific Instruments*, *92*(8), 084710. https://doi.org/10.1063/5.0043648

Sherman, S. M. (1996). Dual response modes in lateral geniculate neurons: Mechanisms and functions. *Visual Neuroscience*, *13*, 205–213. https://doi.org/10.1017/s0952523800007446

Sherman, S. M. (2001). Tonic and burst firing: dual modes of thalamocortical relay. *Trends in Neurosciences*, *24*(2), 122–126. https://doi.org/10.1016/S0166-2236(00)01714-8

Sherman, S. M., & Guillery, R. W. (1996). Functional organization of thalamocortical relays. *Journal of Neurophysiology*, *76*(3), 1367–1395. https://doi.org/10.1152/JN.1996.76.3.1367

Siebner, H. R., Funke, K., Aberra, A. S., Antal, A., Chen, R., Classen, J., Davare, M., Di, V., Fox, P. T., Hallett, M., Karabanov, A. N., Kesselheim, J., Beck, M. M., Koch, G., Liebetanz, D., Meunier, S., Miniussi, C., Paulus, W., Peterchev, A. V, … Ugawa, Y. (2022). Transcranial magnetic stimulation of the brain: What is stimulated? – a consensus and critical position paper. *Clinical Neurophysiology*. https://doi.org/10.1016/J.CLINPH.2022.04.022

Siegle, J. H., Jia, X., Durand, S., Gale, S., Bennett, C., Graddis, N., Heller, G., Ramirez, T. K., Choi, H., Luviano, J. A., Groblewski, P. A., Ahmed, R., Arkhipov, A., Bernard, A., Billeh, Y. N., Brown, D., Buice, M. A., Cain, N., Caldejon, S., … Koch, C. (2021). Survey of spiking in the mouse visual system reveals functional hierarchy. *Nature*, *592*(7852), 86–92. https://doi.org/10.1038/s41586-020-03171-x

Siegle, J. H., López, A. C., Patel, Y. A., Abramov, K., Ohayon, S., & Voigts, J. (2017). Open Ephys: an open-source, plugin-based platform for multichannel electrophysiology. *Journal of Neural Engineering*, *14*(4), 045003. https://doi.org/10.1088/1741-2552/AA5EEA

Sirota, A., Montgomery, S., Fujisawa, S., Isomura, Y., Zugaro, M., & Buzsáki, G. (2008). Entrainment of Neocortical Neurons and Gamma Oscillations by the Hippocampal Theta Rhythm. *Neuron*, *60*(4), 683–697. https://doi.org/10.1016/j.neuron.2008.09.014

Sombeck, J. T., Heye, J., Kumaravelu, K., Goetz, S. M., Peterchev, A. V, Grill, W. M., Bensmaia, S., & Miller, L. E. (2022). Characterizing the short-latency evoked response to intracortical microstimulation across a multi-electrode array. *Journal of Neural Engineering*, *19*(2), 026044. https://doi.org/10.1088/1741-2552/AC63E8

Stoelzel, C. R., Bereshpolova, Y., & Swadlow, H. A. (2009). Stability of Thalamocortical Synaptic Transmission across Awake Brain States. *The Journal of Neuroscience*, *29*(21), 6851–6859.

https://doi.org/10.1523/JNEUROSCI.5983-08.2009

Stringer, C., Pachitariu, M., Steinmetz, N., Reddy, C. B., Carandini, M., & Harris, K. D. (2019). Spontaneous behaviors drive multidimensional, brainwide activity. *Science*, *364*(6437). https://doi.org/10.1126/SCIENCE.AAV7893

Suzuki, M., & Larkum, M. E. (2020). General Anesthesia Decouples Cortical Pyramidal Neurons. *Cell*, *180*(4), 666-676.e13. https://doi.org/10.1016/j.cell.2020.01.024

Swadlow, H. A., & Gusev, A. G. (2001). The impact of "bursting" thalamic impulses at a neocortical synapse. *Nature Neuroscience*, *4*(4), 402–408. https://doi.org/10.1038/86054

Tehovnik, E. J., & Slocum, W. M. (2013). Two-photon imaging and the activation of cortical neurons. *Neuroscience*, *245*(March), 12–25. https://doi.org/10.1016/j.neuroscience.2013.04.022

Tehovnik, E. J., Tolias, A. S., Sultan, F., Slocum, W. M., & Logothetis, N. K. (2006). Direct and indirect activation of cortical neurons by electrical microstimulation. *Journal of Neurophysiology*, *96*(2), 512–521. https://doi.org/10.1152/jn.00126.2006

Terao, Y., & Ugawa, Y. (2002). Basic mechanisms of TMS. *Journal of Clinical Neurophysiology*, *19*(4), 322–343. https://doi.org/10.1097/00004691-200208000-00006

Thibaut, A., Schiff, N., Giacino, J., Laureys, S., & Gosseries, O. (2019). Therapeutic interventions in patients with prolonged disorders of consciousness. *The Lancet Neurology*, *18*, 600–614. https://doi.org/10.1016/S1474-4422(19)30031-6

Timofeev, I., Grenier, F., & Steriade, M. (2001). Disfacilitation and active inhibition in the neocortex during the natural sleep-wake cycle: An intracellular study. *Proceedings of the National Academy of Sciences of the United States of America*, *98*(4), 1924–1929. https://doi.org/10.1073/PNAS.98.4.1924

Urbain, N., Fourcaud-Trocmé, N., Laheux, S., Salin, P. A., & Gentet, L. J. (2019). Brain-State-Dependent Modulation of Neuronal Firing and Membrane Potential Dynamics in the Somatosensory Thalamus during Natural Sleep. *Cell Reports*, *26*(6), 1443-1457.e5. https://doi.org/10.1016/J.CELREP.2019.01.038

Urbain, N., Salin, P. A., Libourel, P.-A., Comte, J.-C., Gentet, L. J., & Petersen, C. C. H. (2015). Whisking-Related Changes in Neuronal Firing and Membrane Potential Dynamics in the Somatosensory Thalamus of Awake Mice. *Cell Reports*, *13*, 647–656. https://doi.org/10.1016/j.celrep.2015.09.029

Usami, K., Matsumoto, R., Kobayashi, K., Hitomi, T., Shimotake, A., Kikuchi, T., Matsuhashi, M., Kunieda, T., Mikuni, N., Miyamoto, S., Fukuyama, H., Takahashi, R., & Ikeda, A. (2015). Sleep modulates cortical connectivity and excitability in humans: Direct evidence from neural activity induced by single-pulse electrical stimulation. *Human Brain Mapping*, *36*(11), 4714–4729. https://doi.org/10.1002/HBM.22948

von Bartheld, C. S., Bahney, J., & Herculano-Houzel, S. (2016). The Search for True Numbers of Neurons and Glial Cells in the Human Brain: A Review of 150 Years of Cell Counting. *J Comp Neurol*, *524*(18), 3865–3895. https://doi.org/10.1002/cne.24040

Vyazovskiy, V. V., Olcese, U., Cirelli, C., & Tononi, G. (2013). Prolonged wakefulness alters neuronal responsiveness to local electrical stimulation of the neocortex in awake rats. *Journal of Sleep Research*, *22*(3), 264. https://doi.org/10.1111/JSR.12009

Walløe, S., Pakkenberg, B., & Fabricius, K. (2014). Stereological estimation of total cell numbers in the human cerebral and cerebellar cortex. *Frontiers in Human Neuroscience*, *8*, 508. https://doi.org/10.3389/FNHUM.2014.00508

Yerkes, R. M., & Dodson, J. D. (1908). The relation of strength of stimulus to rapidity of habit-formation. *Journal of Comparative Neurology and Psychology*, *18*(5), 459–482. https://doi.org/10.1002/CNE.920180503

FIGURE SUPPLEMENTS

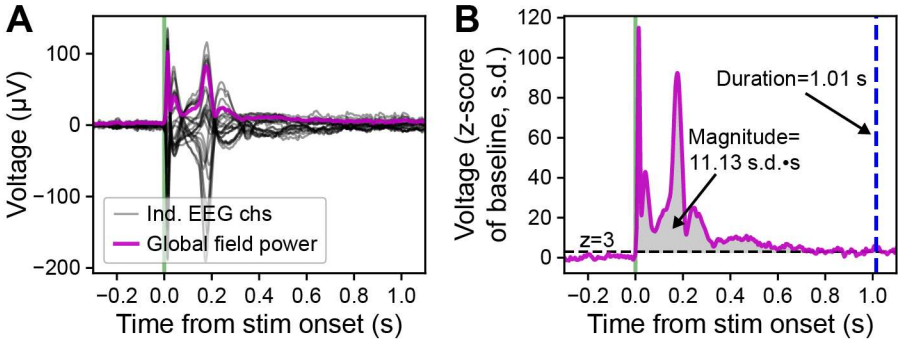

Figure 1-figure supplement 1: Demonstration of duration and magnitude calculation for evoked responses.

(A) Butterfly plot of the ERP (-0.3 to +1.1 s around stimulus onset, green vertical line) from deep stimulation in MOs (black lines). The global field power (magenta line) is calculated as the standard deviation of voltage values across all electrodes at each time sample. Same example as shown in Figure 1C and 1D, bottom left. **(B)** The global field power (baseline z-score; -0.3 to +1.1 s around stimulus onset) from panel **A**. The duration of the evoked response is measured by the length of time the global field power remains above a threshold of three standard deviations above the baseline mean (z=3 s.d., represented by the horizontal, black, dashed line) in the response window from stimulus onset to +2 s after. The duration of this example is 1.01 s, represented by the vertical, dashed, blue line. The magnitude of the evoked response is measured by the area under the curve of the z-scored global field power above the threshold (z=3 s.d.) in the response window from stimulus onset to +2 s after. The magnitude of this example is 11.13 s.d.·s, represented by the gray shaded region.

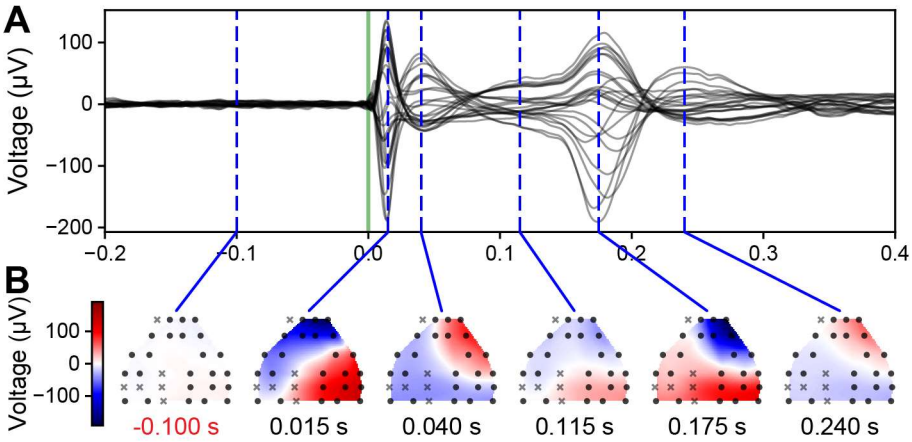

Figure 1-figure supplement 2: Spatial extent of evoked EEG responses in awake, head-fixed mice.

(A) Butterfly plot of the ERP (-0.2 to +0.4 s around stimulus onset, green vertical line) from deep stimulation in MOs. Dashed vertical blue lines indicate the time of the spatial interpolation below. Same example as shown in Figure 1C and 1D bottom left. **(B)** The spatial interpolation of the instantaneous voltage across the surface of the mouse brain sampled by the EEG electrodes. Black circles and gray x-marks represent electrodes that did and did not pass a quality control step, respectively. The white band running across cortex represents the transition between the two polarities of the EEG signals.

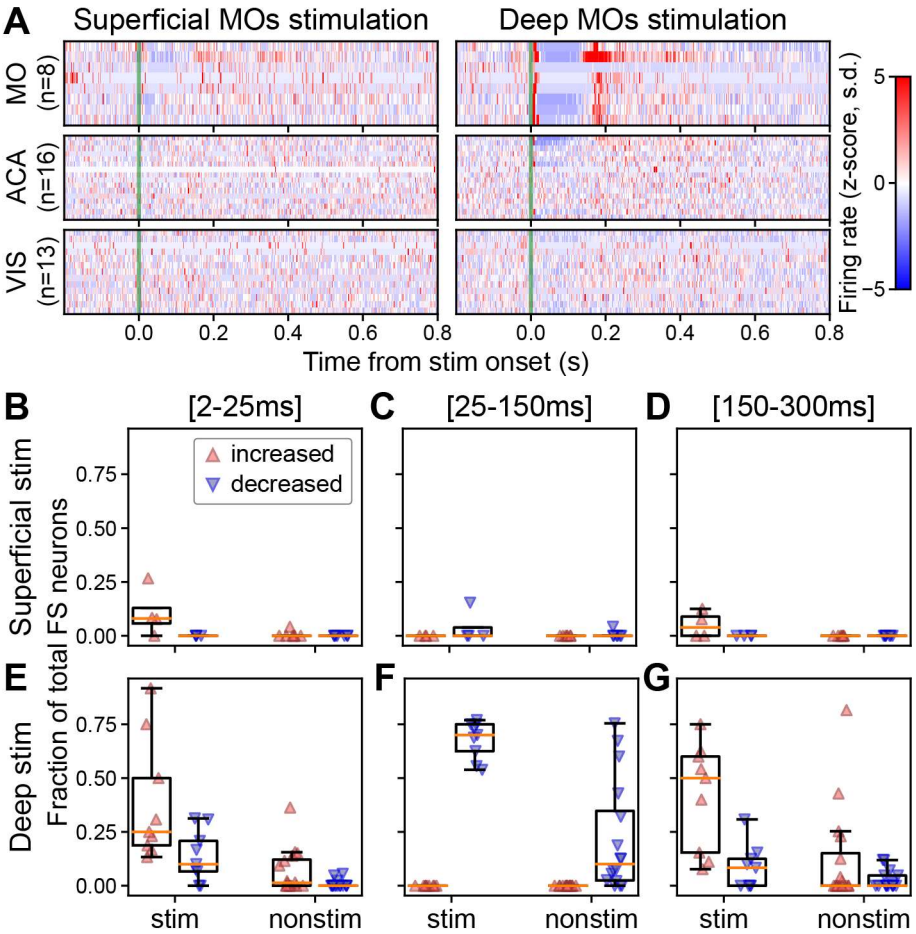

Figure 4-figure supplement 1: The fraction of the FS neuron population that is significantly modulated depends on the depth of stimulation and the temporal window.

(A) Normalized firing rate, reported as a z-score of the average, pre-stimulus firing rate, of FS neurons recorded by the Neuropixels probes targeting cortical areas of interest (left: superficial MOs stimulation; right: deep MOs stimulation). The number of neurons (n) in each area is included along the y-axis. **(B)** Fraction of FS neurons that exhibit a significantly increased (red upward triangle) or decreased (blue downward triangle) response in the first 25 ms for mice that received superficial stimulation. **(C)** Fraction of FS neurons that exhibit a significantly increased or decreased response 25-150 ms following the stimulus. **(D)** Fraction of FS neurons that exhibit a significantly increased or decreased response 150-300 ms following the stimulus. **(E-G)** Same as panels **B-D** but for subjects that received deep stimulation. Data from experiments with superficial cortical stimulation (180 FS neurons from stimulated cortex and 585 FS neurons from non-stimulated cortical regions in N=7 mice) and with deep cortical

stimulation (387 FS neurons from stimulated cortex and 1,422 FS neurons from non-stimulated cortical regions in N=16 mice). Boxplots show median (orange line), 25th, and 75th percentiles; whiskers extend from the box by 1.5x the IQR.

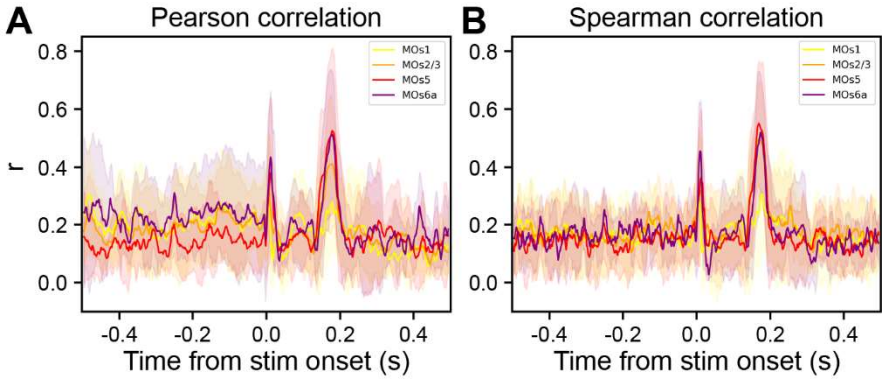

Figure 6-figure supplement 1: ERP is more correlated to CSD of deep, rather than superficial, cortical layers.

Time-resolved correlation of EEG with layer-specific CSD power (traces color coded by layers) at single trial level across all subjects (N=9 mice): **(A)** Pearson correlation, **(B)** Spearman correlation.

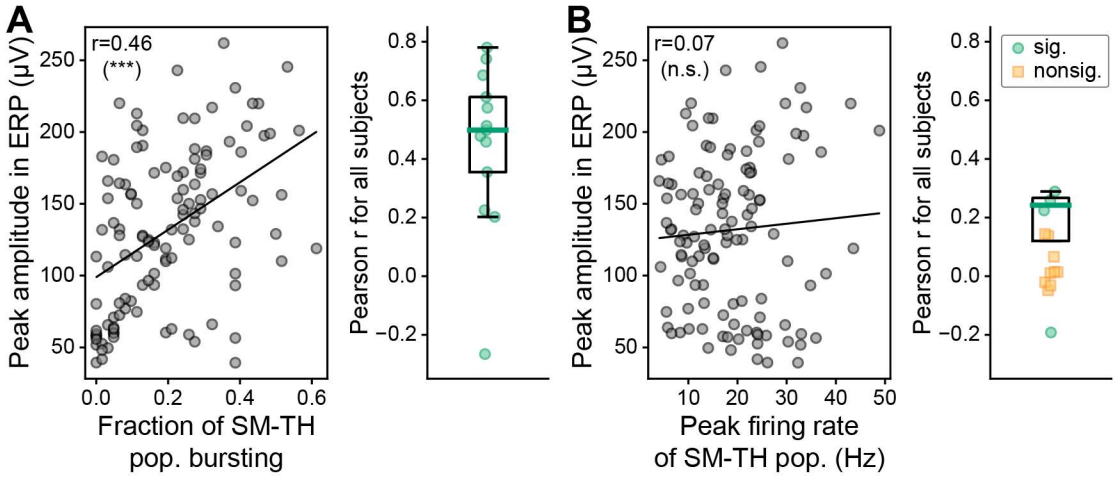

Figure 6-figure supplement 2: The amplitude of the second, late component in the ERP is correlated with the SM-TH bursting, but not the population firing rate.

(A) Left: Pearson correlation between the peak amplitude of the second, late component in the ERP and the fraction of the SM-TH that bursts on a trial-by-trial basis for one example mouse (same subject as in Figure 1D bottom left). **Right:** Same as left, computed for all subjects with deep stimulation (N=12 mice), green circles represent subjects with a significant correlation ($p<0.05$). **(B) Left:** Pearson correlation between the peak amplitude of the second, late component in the ERP and the peak SM-TH population firing rate on a trial-by-trial basis for one example mouse. **Right:** The correlation value (Pearson r) for all subjects with deep stimulation (N=12 mice), green circles represent subjects with a significant correlation ($p<0.05$) and yellow squares represent subjects with a non-significant correlation. Boxplots show median (green line), 25th, and 75th percentiles; whiskers extend from the box by 1.5x the IQR. * Weak evidence to reject null hypothesis ($0.05 > p > 0.01$), ** strong evidence to reject null hypothesis ($0.01 > p > 0.001$), *** very strong evidence to reject null hypothesis ($0.001 > p$).